

PREPARED FOR SUBMISSION TO JCAP

# Thin accretion disk signatures in hybrid metric-Palatini $f(R)$ -gravity

P I Dyadina,<sup>a</sup> N A Avdeev<sup>a</sup>

<sup>a</sup>Sternberg Astronomical Institute, Lomonosov Moscow State University,  
Universitetsky Prospekt, 13, Moscow, Russia

E-mail: [guldur.anwo@gmail.com](mailto:guldur.anwo@gmail.com), [NAAvdeev1995@mail.ru](mailto:NAAvdeev1995@mail.ru)

**Abstract.** In the present work, accretion onto a spherically symmetric black hole in the hybrid metric-Palatini  $f(R)$ -gravity is considered. The Novikov-Thorne model for a relativistic thin accretion disk is used. The energy flux, temperature distribution, emission spectrum and energy conversion efficiency of accretion disks around such black holes are numerically calculated. A comparison with the results for a Schwarzschild black hole is made and conclusions about the viability of the model are drawn. As a result, it is obtained that the accretion disks around black holes in hybrid metric-Palatini  $f(R)$ -gravity are colder and less luminous than in general relativity.

**Keywords:** accretion, spherical symmetric black hole, hybrid metric-Palatini  $f(R)$ -gravity, modified theories of gravity

---

## Contents

<b>1</b>	<b>Introduction</b>	<b>1</b>
<b>2</b>	<b>Hybrid <math>f(R)</math>-gravity</b>	<b>2</b>
<b>3</b>	<b>Thin accretion disk model</b>	<b>4</b>
<b>4</b>	<b>Numerical results</b>	<b>6</b>
<b>5</b>	<b>Properties of thin accretion discs</b>	<b>7</b>
5.1	Case $V = 0$	7
5.1.1	Energy flux	8
5.1.2	Emission spectra.	8
5.1.3	Temperature.	9
5.1.4	Efficiency.	12
5.2	Case $V = -\frac{\mu^2}{2}\phi^2 + \frac{\zeta}{4}\phi^4$	12
5.2.1	Energy flux	13
5.2.2	Emission spectra.	14
5.2.3	Temperature.	18
5.2.4	Efficiency.	18
<b>6</b>	<b>Discussion</b>	<b>22</b>
<b>7</b>	<b>Conclusions</b>	<b>24</b>

---

## 1 Introduction

At the beginning of the XX century, general relativity (GR) replaced Newton's theory of gravity, offering solutions to long-standing unresolved issues. GR has since remained the generally accepted theory of gravity. However, as physics progressed, new challenges emerged that could not be addressed by GR alone, including dark matter [1, 2], dark energy [3–7], quantum gravity and inflation [8–10]. One of the ways to solve these problems is to search for a theory of gravity that go beyond the scope of GR.

Among the various modified gravitational theories, one such theory is  $f(R)$ -gravity [11–14], where the scalar curvature  $R$  is replaced by an arbitrary function of the Ricci scalar. The large family of  $f(R)$ -theories can be divided into two classes: metric and Palatini ones. In the metric approach the only variable is the metric, while in the Palatini approach an additional variable is the independent affine connection.

Within the framework of the metric approach, it is possible to successfully describe the dynamics of the modern universe. However, it encounters difficulties in explaining the dynamics within the solar system [15–17]. Nevertheless, there are a number of viable models that can overcome these difficulties [18–20].

Another approach is the Palatini approach, which assumes the affine connection is independent of the metric [21, 22]. However, this modification also faces limitations when it comes to describing observational data [23, 24].

To overcome these challenges, hybrid metric-Palatini  $f(R)$ -gravity was developed [25, 26, 27]. This theory combines the advantages of the metric and Palatini approaches while avoids their shortcomings. Hybrid  $f(R)$ -gravity offers simultaneous explanations for cosmological [28–30] and solar system dynamics [31, 32] without the need for screening mechanisms. Moreover, this model has a scalar-tensor representation, simplifying its study. Hybrid  $f(R)$ -gravity was explored in the context of solar system dynamics [32], binary pulsars [33, 34], galactical scales [35], gravitational waves [36, 37] and even in the derivation of wormhole and black hole solutions [38, 39, 40].

In this paper, our focus is on studying accretion onto a symmetric black hole within the hybrid  $f(R)$ -gravity. Accretion, the process of matter infall onto a black hole, is highly sensitive to the gravitational theory’s peculiarities, making it a valuable testbed for exploring new results and constraints for this model. Historically, the first accretion model was created by N. Shakura and R. Sunyaev [41]. However, the first model which takes into account relativistic effects was developed by I. Novikov and K. Thorne [42, 43]. Previously, many modified theories of gravity have already been investigated by considering accretion disks [44–49].

We employ a numerical solution for the static spherical symmetric black hole metric in hybrid  $f(R)$ -gravity [39] to calculate the energy flux, luminosity, and temperature within the Novikov-Thorne model. We compare our results with calculations performed for a Schwarzschild black hole in GR. Our analysis considers different values of the background scalar field, first derivative of the scalar field, scalar field mass, and different their interconnections. We examine two cases: one with a Higgs-type potential  $V(\phi) = -\frac{\mu^2}{2}\phi^2 + \frac{\zeta}{4}\phi^4$  and another without any potential ( $V = 0$ ). In the conclusion, we discuss the viable aspects of the hybrid  $f(R)$ -theory.

The article is organized into seven sections. The first and last are the introduction and conclusion respectively. The second section provides a description of the hybrid  $f(R)$ -model and its scalar-tensor representation. In the third section, we present the Novikov-Thorne model. The fourth section outlines the numerical calculations for the static spherical symmetric black hole metric. In the fifth section the results of numerical calculating for accretion in hybrid  $f(R)$ -gravity are presented. In the sixth section we discuss about obtained results of this research. The conclusion summarizes our findings.

Throughout this paper the Greek indices  $(\mu, \nu, \dots)$  run over 0, 1, 2, 3 and the signature is  $(-, +, +, +)$ . All calculations are performed in the CGS system.

## 2 Hybrid $f(R)$ -gravity

In this section, we discuss the fundamental characteristics of hybrid  $f(R)$ -theory and introduce mathematical background of this theory. The action is formulated as follows [25, 26]:

$$S = \frac{1}{2k^2} \int d^4x \sqrt{-g} [R + f(\mathfrak{R})] + S_m, \quad (2.1)$$

where  $k^2 = \frac{8\pi G}{c^4}$ ,  $G$  is the gravitational constant,  $c$  is the speed of light,  $g = \det\{g_{\mu\nu}\}$  is the determinant of the metric,  $R$  and  $\mathfrak{R}$  are the metric and Palatini curvatures respectively and  $S_m$  is the matter action. The first part of the action, the metric curvature  $R$ , corresponds to the Einstein-Hilbert action. The second part consists of general function of the Palatini curvature and includes all deviations from GR.

The general form of scalar curvature expressions is the same:

$$\begin{aligned}
R &= g^{\mu\nu} R_{\mu\nu} \equiv g^{\mu\nu} \left( \Gamma_{\mu\nu,\alpha}^\alpha - \Gamma_{\mu\alpha,\nu}^\alpha + \Gamma_{\alpha\lambda}^\alpha \Gamma_{\mu\nu}^\lambda - \Gamma_{\mu\lambda}^\alpha \Gamma_{\alpha\nu}^\lambda \right), \\
\mathfrak{R} &= g^{\mu\nu} \mathfrak{R}_{\mu\nu} \equiv g^{\mu\nu} \left( \hat{\Gamma}_{\mu\nu,\alpha}^\alpha - \hat{\Gamma}_{\mu\alpha,\nu}^\alpha + \hat{\Gamma}_{\alpha\lambda}^\alpha \hat{\Gamma}_{\mu\nu}^\lambda - \hat{\Gamma}_{\mu\lambda}^\alpha \hat{\Gamma}_{\alpha\nu}^\lambda \right).
\end{aligned} \tag{2.2}$$

However, in the metric approach, curvature depends only on the metric, while in the Palatini approach curvature is a function of both the metric and the affine connection. Like other metric and Palatini f(R)-gravity models, it is possible to represent hybrid f(R)-gravity in a scalar-tensor form. Let us to introduce an auxiliary field  $A$  that allows to write the action as follows:

$$S = \frac{1}{2k^2} \int d^4x \sqrt{-g} [R + f(A) + f_A \cdot (\mathfrak{R} - A)] + S_m, \tag{2.3}$$

where  $f_A = \frac{df}{dA}$ . Then we can introduce the scalar field  $\phi \equiv f_A$  and the potential  $V(\phi) \equiv Af_A - f(A)$ , which consist of kinetic and potential parts. After mathematical transformations we obtain the scalar-tensor representation of the hybrid f(R)-gravity action:

$$S = \frac{1}{2k^2} \int d^4x \sqrt{-g} [R + \phi \mathfrak{R} - V(\phi)] + S_m. \tag{2.4}$$

To obtain the field equations, it is necessary to vary the action with respect to all variables: the metric tensor  $g_{\mu\nu}$ , the scalar field  $\phi$  and the affine connection  $\hat{\Gamma}_{\mu\nu}^\alpha$ . Thus the field equations take the following form:

$$\begin{aligned}
R_{\mu\nu} + \phi \mathfrak{R}_{\mu\nu} - \frac{1}{2} (R + \phi \mathfrak{R} - V) g_{\mu\nu} &= k^2 T_{\mu\nu}, \\
\mathfrak{R} - V_\phi &= 0, \\
\hat{\nabla}_\alpha (\sqrt{-g} \phi g^{\mu\nu}) &= 0,
\end{aligned} \tag{2.5}$$

where  $T_{\mu\nu}$  is the energy-momentum tensor, and  $V_\phi \equiv \frac{dV}{d\phi}$ . It is necessary to emphasize that there is no torsion in hybrid f(R)-gravity. Consequently, the final equation can be resolved, revealing that the independent connection corresponds to the Levi-Civita connection of the metric  $h_{\mu\nu} = \phi g_{\mu\nu}$ . By employing the solution of this equation, a connection between the metric and the Palatini curvatures can be expressed:

$$\mathfrak{R}_{\mu\nu} = R_{\mu\nu} + \frac{3}{2\phi^2} \partial_\mu \phi \partial_\nu \phi - \frac{1}{\phi} \left( \nabla_\mu \nabla_\nu \phi + \frac{1}{2} g_{\mu\nu} \nabla_\alpha \nabla^\alpha \phi \right). \tag{2.6}$$

This connection allows to rewrite the action without Palatini terms [25, 26]:

$$S = \frac{1}{2k^2} \int d^4x \sqrt{-g} \left[ (1 + \phi) R + \frac{3}{2\phi} \partial_\mu \phi \partial^\mu \phi - V(\phi) \right] + S_m. \tag{2.7}$$

Thus, the action of hybrid f(R)-gravity in the scalar-tensor representation has been obtained.

Taking into account expressions (2.5), it is possible to derive the scalar-tensor form of the field equations:

$$\frac{1}{1 + \phi} \left[ k^2 \left( T_{\mu\nu} - \frac{1}{2} g_{\mu\nu} T \right) + \frac{1}{2} g_{\mu\nu} (V + \nabla_\alpha \nabla^\alpha \phi) + \nabla_\mu \nabla_\nu \phi - \frac{3}{2\phi} \partial_\mu \phi \partial_\nu \phi \right] = R_{\mu\nu}, \tag{2.8}$$

$$-\nabla_\mu \nabla^\mu \phi + \frac{1}{2\phi} \partial_\mu \phi \partial^\mu \phi + \frac{\phi[2V - (1 + \phi)V_\phi]}{3} = \frac{\phi k^2}{3} T. \tag{2.9}$$

From here onwards, the field equations are considered in this form.

### 3 Thin accretion disk model

An accretion disk is an astrophysical structure that forms near a massive object, representing diffuse material orbiting around the central body. In this article only thin accretion discs are considered. The general model of such disks was developed by N. Shakura and R. Sunyaev [41] and later extended by I. Novikov, K. Thorne and D. Page [42, 43]. A thin accretion disk is characterized by the fact that its vertical size,  $h$ , is negligible compared to its horizontal size,  $h \ll r$ . In such structures, particles move along Keplerian orbits, and the accretion disk is located in the equatorial plan of the compact body. Moreover, the thin accretion disk model implies a steady state. Thus, the accretion mass rate,  $\dot{M}_0$ , is assumed to be constant over time. Additionally, in the steady-state model the accreting matter is in thermodynamical equilibrium [45].

To study the electromagnetic properties of an accretion disk, it is first necessary to study the geometry of space in which particles move near a compact object [44]. The geodesic motion of test particles moving around a massive body is governed by the Lagrangian:

$$L = \frac{1}{2} g_{\mu\nu} \dot{x}^\mu \dot{x}^\nu, \quad (3.1)$$

where the dot means the derivative with respect to  $\tau$ , which is an affine parameter along the geodesic  $x^\mu(\tau)$ ;  $g_{\mu\nu}$  is the metric of a static, spherically symmetric space-time:

$$ds^2 = g_{00}dt^2 + g_{11}dr^2 + g_{22}d\theta^2 + g_{33}d\varphi^2, \quad (3.2)$$

for which the elements  $g_{00}, g_{11}, g_{22}, g_{33}$  only depend on the radial coordinate  $r$ . We also use an equatorial approximation, implying that  $|\theta - \pi/2| \ll 1$ . To derive the main features of the thin accretion disk, it becomes essential to define the specific energy  $\tilde{E}$  and the specific angular momentum  $\tilde{L}$  using the Euler-Lagrange equations [42]:

$$g_{00}\dot{t} = \tilde{E}, \quad (3.3)$$

$$g_{22}\dot{\varphi} = \tilde{L}. \quad (3.4)$$

Here  $\tilde{E} = E/m_0c^2$  and  $\tilde{L} = L/m_0c$ , where  $E$  represents the total energy of the particle in its orbit,  $m_0c^2$  is the rest mass energy of this particle and  $L$  is the angular momentum of the particle.

Another important characteristic of the accretion disk is the effective potential  $V_{eff}(r)$ . It can be defined from the relation  $2L = -1$ , taking into account (3.3) and (3.4):

$$-g_{00}g_{11}\dot{r}^2 + V_{eff}(r) = \tilde{E}^2. \quad (3.5)$$

Then the effective potential is defined as

$$V_{eff}(r) = -g_{00} \left( 1 + \frac{\tilde{L}^2}{g_{33}} \right). \quad (3.6)$$

The circular orbit passes where the minimum of the effective potential is located. If there is no minimum (i.e., the potential has a "smooth" shape), then the circular orbits are unstable for a given moment. Therefore, for stable circular orbits, conditions  $V_{eff}(r) = 0$  and  $V_{eff,r}(r) = 0$  must be satisfied. This makes it possible to determine the specific energy, specific angular

momentum, and angular velocity  $\Omega$  of particles moving within the gravitational potential of a massive object:

$$\tilde{E} = -\frac{g_{00}}{\sqrt{-g_{00} - g_{33}\Omega^2}}, \quad (3.7)$$

$$\tilde{L} = \frac{g_{33}\Omega}{\sqrt{-g_{00} - g_{33}\Omega^2}}, \quad (3.8)$$

$$\Omega = \frac{d\varphi}{dt} = \sqrt{\frac{-g_{00,r}}{-g_{33,r}}}. \quad (3.9)$$

The condition  $V_{eff,rr}(r) = 0$  determines the radius of the innermost stable circular orbit  $r_{isco}$ . This leads to the following equation:

$$\tilde{E}^2 g_{33,rr} + \tilde{L}^2 g_{00,rr} + (g_{00}g_{33})_{,rr} = 0. \quad (3.10)$$

Solving this equation with respect to  $r$  and taking into account expressions (3.7, 3.8), we obtain the  $r_{isco}$ .

A key feature of an accretion disk is its accretion efficiency, a measure which signifies the capacity of the central body to transmute rest mass into outgoing radiation. This measure is established as the proportion of the photon energy rate that escapes from the disk's surface to infinity to the rate at which mass-energy is transported to the black hole. If all emitted photons can escape to infinity, the efficiency can be expressed in terms of the specific energy defined at  $r_{isco}$  [42, 43]:

$$\eta = 1 - \tilde{E}_{ms}. \quad (3.11)$$

Schwarzschild black holes have an efficiency of approximately 6%, while for extreme rotating Kerr black holes,  $\eta \approx 42\%$ . It is important to note that the photon capture by the black hole can influence the efficiency. For instance, a Kerr black hole with photon capture has an efficiency of 40% [50].

One of the main parameters that characterize the spectrum of an accretion disk is the time averaged energy flux emitted from the surface of the disk. It can be obtained from the conservation equations  $\nabla_\mu E^\mu = 0$  and  $\nabla_\mu J^\mu = 0$ . The radiation flux per unit area can be expressed in terms of the specific energy, angular momentum and the angular velocity of the particles orbiting in the disk as follows:

$$F(r) = -\frac{\dot{M}_0}{4\pi\sqrt{-g}} \frac{\Omega_{,r}}{(\tilde{E} - \Omega\tilde{L})^2} \int_{r_{isco}}^r (\tilde{E} - \Omega\tilde{L})\tilde{L}_{,r} r dr, \quad (3.12)$$

where  $\dot{M}_0$  is the mass accretion rate. This quantity measures the rate at which the rest mass of the particles streams inward through the disk with respect to the coordinate time.<sup>1</sup>

The steady-state thin disk model includes a condition that the accreting matter is assumed to be in thermodynamic equilibrium. As a result, an ideal black body model is applicable in describing the radiation from the disk's surface, and the energy flux can be derived from the Stefan-Boltzmann law,  $F(r) = \sigma T(r)^4$ , where  $\sigma$  is the Stefan-Boltzmann

---

<sup>1</sup>In the original article by D. Page and K. Thorne [42], this formula (3.12) was obtained for cylindrical coordinates. Therefore, when working in a spherical coordinate system, it is important to take into account the Jacobian for the transition from one system to another.

constant. Therefore, the observed luminosity has a redshifted black body spectrum as follows [51]:

$$L(\nu) = \frac{2}{c^2} \cos \gamma \int_{r_i}^{r_f} \int_0^{2\pi} \frac{\nu_e^3 r d\varphi dr}{\exp(h\nu_e/kT) - 1}. \quad (3.13)$$

Here  $d$  denotes the distance to the source,  $\gamma$  represents the disk inclination angle,  $r_i$  and  $r_f$  are the radii of the disk's inner and outer edge, respectively.  $\nu_e = \nu(1+z)$  denotes the emitted frequency, and the redshift factor is defined as:

$$1+z = \frac{1 + \Omega r \sin \varphi \sin \gamma}{\sqrt{-g_{00} - g_{33}\Omega^2}}, \quad (3.14)$$

where we neglect the light bending [52].

## 4 Numerical results

The spherical symmetric space-time outside massive objects can be described by the following line element:

$$ds^2 = -e^{\nu(r)} dt^2 + e^{\lambda(r)} dr^2 + r^2(d\theta^2 + \sin^2 \theta d\varphi^2). \quad (4.1)$$

The metric functions  $\nu(r)$  and  $\lambda(r)$  depend only on the radial coordinate  $r$ , with the condition  $0 \leq r < \infty$ . Taking into account the metric (4.1), the field equations (2.8) and (2.9) can be represented in the following form:

$$\frac{d\phi}{d\xi} = -\frac{U}{\xi^2}, \quad (4.2)$$

$$\frac{dM_{eff}}{d\xi} = \frac{(1 - M_{eff}\xi)[\xi^2 dU/d\xi + 3U^2/4\phi - 2\xi U] + M_{eff}\xi^3(1 + \phi) - v}{\xi^4(1 + \phi + U/2\xi)} - \frac{M_{eff}}{\xi}, \quad (4.3)$$

$$\frac{d\nu}{d\xi} = -\frac{\xi - \left\{ \frac{U(\xi)[8\phi + 3U(\xi)/\xi]}{4\phi(1+\phi)} + \xi \right\} [1 - \xi M_{eff}(\xi)] - \frac{v(\phi)}{\xi(1+\phi)}}{\xi^2 [1 - \xi M_{eff}(\xi)] \left[ 1 + \frac{U(\xi)}{2\xi(1+\phi)} \right]}, \quad (4.4)$$

$$\frac{d^2\nu}{d\xi^2} = \frac{(1 - \frac{\xi}{2} \frac{d\nu}{d\xi})(-\xi \frac{dM_{eff}}{d\xi} - M_{eff})}{\xi(1 - \xi M_{eff})} - \frac{5U(\xi)^2}{2\xi^4\phi(1 + \phi)} + \frac{2U}{\xi^3(1 + \phi)} \quad (4.5)$$

$$- \frac{2}{\xi^4(1 + \phi)(1 - \xi M_{eff})} \left\{ \frac{2\phi}{3} [2v - (1 + \phi)v_\phi] + v \right\} - \frac{1}{2} \left( \frac{d\nu}{d\xi} \right)^2 + \frac{1}{\xi} \frac{d\nu}{d\xi}, \quad (4.6)$$

$$\begin{aligned} \frac{dU(\xi)}{d\xi} &= \frac{\frac{\xi^2 U(\xi)}{2} [\xi \frac{dM_{eff}(\xi)}{d\xi} + M_{eff}(\xi)] - \frac{2\phi}{3} [2v(\phi) - (1 + \phi)v_\phi(\phi)]}{\xi^2(1 - \xi M_{eff}(\xi))} \\ &\quad - \frac{U(\xi)}{2} \frac{d\nu}{d\xi} - \frac{1}{\xi^2} \frac{U^2(\xi)}{2\phi} + \frac{2U(\xi)}{\xi}. \end{aligned} \quad (4.7)$$

To obtain these equations, the following transitions to dimensionless variables were used

$$\xi = \frac{2GM_{BH}}{c^2 r}, \quad \frac{d\phi}{dr} = \frac{c^2}{2GM_{BH}} U, \quad V(\phi) = 2 \left( \frac{c^2}{2GM_{BH}} \right)^2 v(\phi). \quad (4.8)$$

where  $M_{BH}$  is the black hole mass. The metric function  $e^{-\lambda(r)}$  is redefined as

$$e^{-\lambda} = 1 - \frac{2GM_{BH}M_{eff}(r)}{c^2r}. \quad (4.9)$$

These field equations were obtained in the article [39]. Then authors found numerical solutions for these field equations. In our work, we repeat the numerical analysis using integration methods from Python's scipy library. For the solution, the fixed initial conditions

$$M_{eff}(0) = 1, \quad \nu(0) = 0, \quad \nu'(0) = 0 \quad (4.10)$$

were taken into account, and arbitrary numerical values for

$$u(0) = u_0, \quad \phi(0) = \phi_0 \quad (4.11)$$

were used.

The details of the calculations of the metric can be found in the article [39].

## 5 Properties of thin accretion discs

Now, we are ready to investigate the properties of thin accretion disks around black holes in hybrid metric-Palatini f(R)-gravity and compare the results with the Schwarzschild predictions. We consider two cases: a case without potential  $V = 0$  and a case where potential takes the Higgs-type form  $V = -\frac{\mu^2}{2}\phi^2 + \frac{\zeta}{4}\phi^4$ .

### 5.1 Case $V = 0$

In the case  $V = 0$ , the metric of the hybrid f(R)-gravity includes two model parameters: the initial value of the scalar field,  $\phi_0$ , and the initial value of its derivative  $u_0$ . We consider three cases:

1. fixed  $\phi_0 = 1$  and range of  $u_0 = [4 \times 10^{-9}; 6.4 \times 10^{-8}]$ ,
2. fixed  $u_0 = 5.12 \times 10^{-7}$  and range  $\phi_0 = [0.5; 8]$ ,
3. a connection between  $\phi_0$  and  $u_0$  obtained from the post-Newtonian analysis. This connection has the following form:

$$u_0 = \frac{2GM\phi_0}{3c^2r^2}. \quad (5.1)$$

It can be obtained from the expression for scalar perturbation  $\varphi = \frac{-2GM\phi_0 e^{-m\phi r}}{3c^2r}$  [32]. In this case, we consider  $\phi_0 < 4 \times 10^{-5}$  [31]. This limit was imposed on the initial value of the scalar field using the data from the Cassini experiment [53].

The first two cases are chosen due to the fact that such black holes were studied in the article [39], where spherical symmetric solution was obtained. The choice of the last case has the following reason: we take the initial value of the scalar field at a sufficiently large distance from the black hole. At this distance, the gravitational field is quite weak, therefore we can use the results of the post-Newtonian analysis.

Further we present the results of the analysis of figures in accordance with these cases.



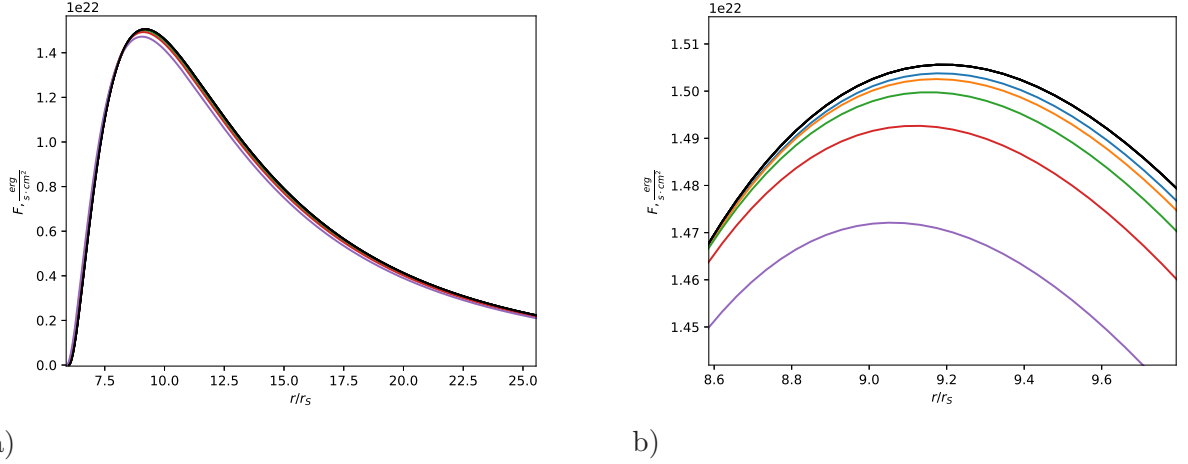


**Figure 1.** Case  $V = 0$ . The energy flux  $F(r)$  of a disk around a static black hole with mass accretion rate  $\dot{M} = 4.72 \times 10^{18} g/s$  and mass  $M = 14.8 M_{\odot}$  for different values of  $u_0$  and fixed  $\phi_0 = 1$  as functions of the normalized radial coordinate  $r/r_s$ . The black curve corresponds to the Schwarzschild black hole. The initial value of scalar field derivative is taken to be:  $u_0 = 4 \times 10^{-9}$  (blue curve),  $u_0 = 8 \times 10^{-9}$  (orange curve),  $u_0 = 1.6 \times 10^{-8}$  (green curve),  $u_0 = 3.2 \times 10^{-8}$  (red curve),  $u_0 = 6.4 \times 10^{-8}$  (purple curve). The figure on the right panel is a zoom version of the left one.

### 5.1.1 Energy flux

1. The effects of hybrid f(R)-gravity on the energy flux across the disk's surface are presented in Figures (1) in this case. Here, all curves lie below the Schwarzschild solution. Additionally, as  $u_0$  increases, the peak value of the energy flux decreases. The largest discrepancy in the peak energy flux within this range of parameters is no more than 2.5 % relative to the Schwarzschild value.
2. In Figure (2), we observe a decline in the maximum energy flux as  $\phi_0$  decreases. All curves again sit beneath the Schwarzschild one. However, in this case, the difference between the maxima is much more noticeable, reaching up to 95%. We assume that such relationships between  $\phi_0$  and  $u_0$  may not be realistic, since they lead to an unrealistic picture of the energy flux.
3. The most realistic picture arises when the parameters are considered within the limits imposed from the solar system. As we can see in the Figure (3) in this case the result is close to Schwarzschild curve.

### 5.1.2 Emission spectra.

1. In Figures (4), we display the disk spectra for accretion disk around black holes and compare it with the emission spectra for the Schwarzschild black hole. In the case of a fixed  $\phi_0$ , the luminosity decreases with increasing  $u_0$ .
2. For a fixed  $u_0$ , the luminosity decreases with decreasing  $\phi_0$ . It can be seen on Figures (5).
3. The curve obtained in the frameworks of solar system limitations looks the most realistic. The two curves are almost identical in Figure (6).

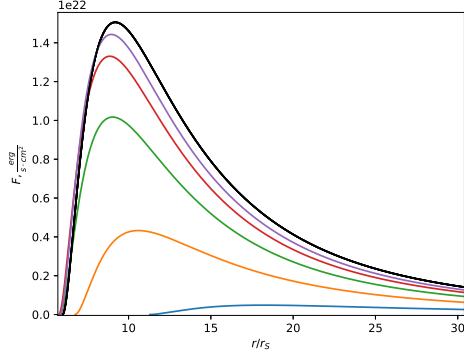


**Figure 2.** Case  $V = 0$ . The energy flux  $F(r)$  of a disk around a static black hole with mass accretion rate  $\dot{M} = 4.72 \times 10^{18} g/s$  and mass  $M = 14.8 M_\odot$  for different values of  $\phi_0$  and fixed  $u_0 = 5.12 \times 10^{-7}$  as functions of the normalized radial coordinate  $r/r_s$ . The black curve corresponds to the Schwarzschild black hole. The initial value of scalar field is taken to be:  $\phi_0 = 0.5$  (blue curve),  $\phi_0 = 1$  (orange curve),  $\phi_0 = 2$  (green curve),  $\phi_0 = 4$  (red curve),  $\phi_0 = 8$  (purple curve).

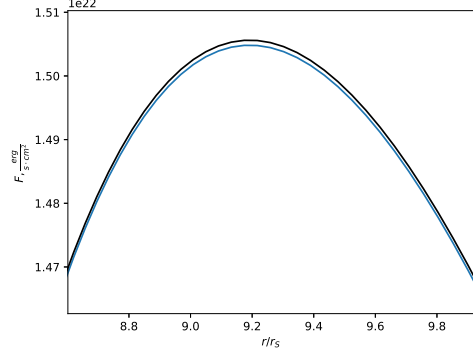
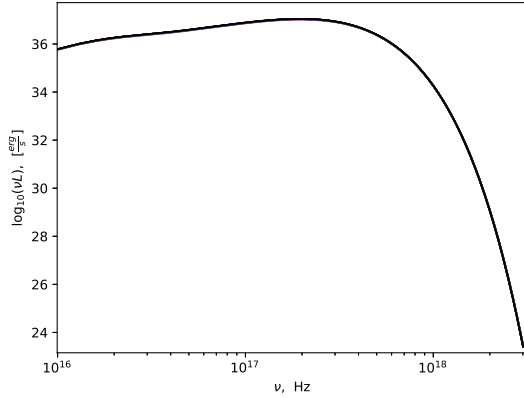
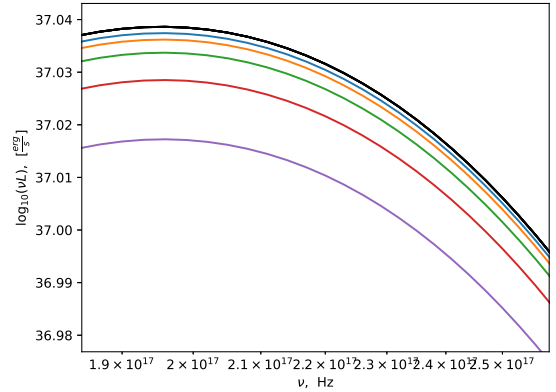


**Figure 3.** Case  $V = 0$ . The energy flux  $F(r)$  of a disk around a static black hole with mass accretion rate  $\dot{M} = 4.72 \times 10^{18} g/s$  and mass  $M = 14.8 M_\odot$  for values of  $\phi_0 = 4 \times 10^{-5}$  and  $u_0 = 2.2 \times 10^{-17}$  as functions of the normalized radial coordinate  $r/r_s$ . The black curve corresponds to the Schwarzschild black hole.



a)



b)

**Figure 4.** Case  $V = 0$ . The emission spectrum  $\nu L(\nu)$  of the accretion disk around a static black hole with mass accretion rate  $\dot{M} = 4.72 \times 10^{18} g/s$  and mass  $M = 14.8 M_\odot$  for different values of  $u_0$  and fixed  $\phi_0 = 1$  as functions of frequency  $\nu$ . The black curve corresponds to the Schwarzschild black hole. The initial value of scalar field derivative is taken to be:  $u_0 = 4 \times 10^{-9}$  (blue curve),  $u_0 = 8 \times 10^{-9}$  (orange curve),  $u_0 = 1.6 \times 10^{-8}$  (green curve),  $u_0 = 3.2 \times 10^{-8}$  (red curve),  $u_0 = 6.4 \times 10^{-8}$  (purple curve). The figure on the right panel is a zoom version of the left one.

### 5.1.3 Temperature.

Since the temperature is related to the energy flux through the Stefan-Boltzmann constant, the results for the effective temperature are no different from the conclusions made for the

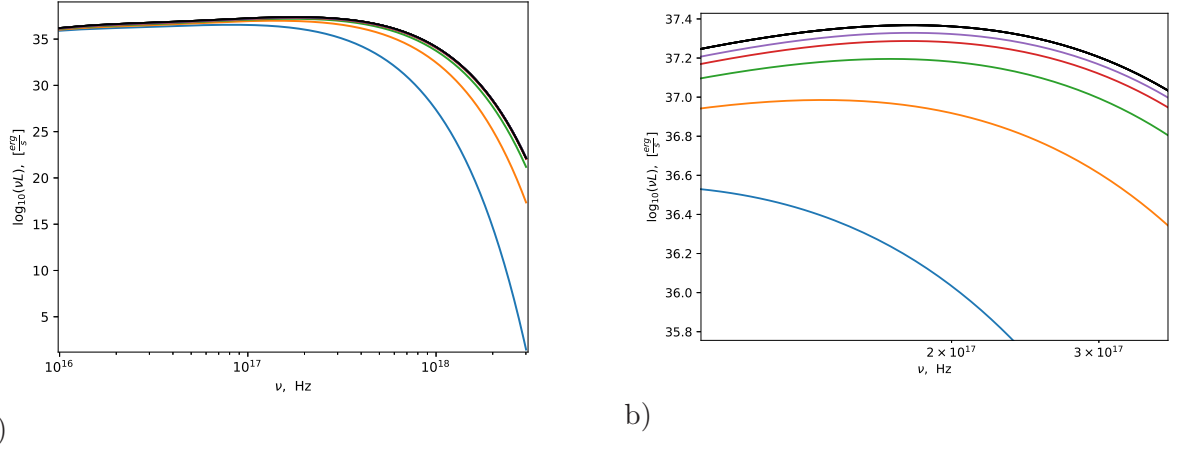


**Figure 5.** Case  $V = 0$ . The emission spectrum  $\nu L(\nu)$  of the accretion disk around a static black hole with mass accretion rate  $\dot{M} = 4.72 \times 10^{18} g/s$  and mass  $M = 14.8 M_{\odot}$  for different values of  $\phi_0$  and fixed  $u_0 = 5.12 \times 10^{-7}$  as functions of frequency  $\nu$ . The black curve corresponds to the Schwarzschild black hole. The initial value of scalar field is taken to be:  $\phi_0 = 0.5$  (blue curve),  $\phi_0 = 1$  (orange curve),  $\phi_0 = 2$  (green curve),  $\phi_0 = 4$  (red curve),  $\phi_0 = 8$  (purple curve).

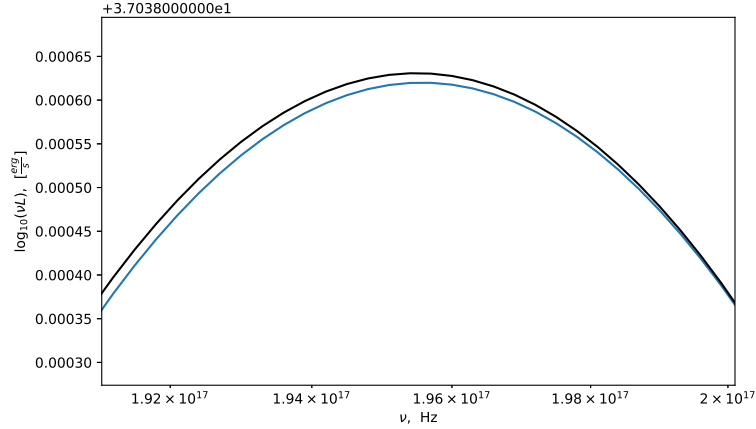
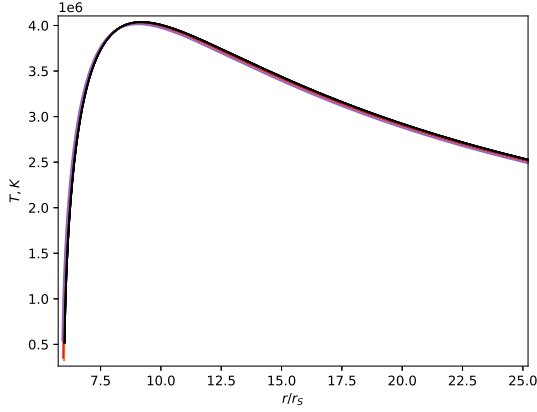


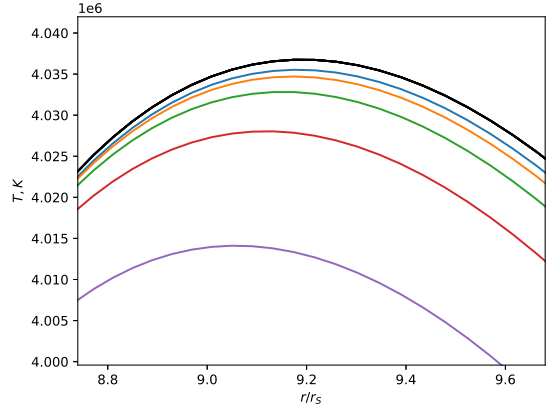
**Figure 6.** Case  $V = 0$ . The emission spectrum  $\nu L(\nu)$  of the accretion disk around a static black hole with mass accretion rate  $\dot{M} = 4.72 \times 10^{18} g/s$  and mass  $M = 14.8 M_{\odot}$  for values of  $\phi_0 = 4 \times 10^{-5}$  and  $u_0 = 2.2 \times 10^{-17}$  as functions of frequency  $\nu$ . The black curve corresponds to the Schwarzschild black hole.

energy flux.

Generally speaking, temperature can serve as an excellent indicator to test a theory because its value can be determined from observational data [54]. Unfortunately, all known accreting systems have a nonzero Kerr parameter. And even a small deviation of this parameter from zero (for example, 0.14) does not allow us to check the results found for a static spherically symmetric black hole with the obtained observational data. Thus, the observational test of the theory is possible only in the case of obtaining the Kerr-type solution and



a)



b)

**Figure 7.** Case  $V = 0$ . The temperature distribution  $T(r)$  of a disk around a static black hole with mass accretion rate  $\dot{M} = 4.72 \times 10^{18} g/s$  and mass  $M = 14.8M_{\odot}$  for different values of  $u_0$  and fixed  $\phi_0 = 1$  as functions of the normalized radial coordinate  $r/r_s$ . The black curve corresponds to the Schwarzschild black hole. The initial value of scalar field derivative is taken to be:  $u_0 = 4 \times 10^{-9}$  (blue curve),  $u_0 = 8 \times 10^{-9}$  (orange curve),  $u_0 = 1.6 \times 10^{-8}$  (green curve),  $u_0 = 3.2 \times 10^{-8}$  (red curve),  $u_0 = 6.4 \times 10^{-8}$  (purple curve). The figure on the right panel is a zoom version of the left one.

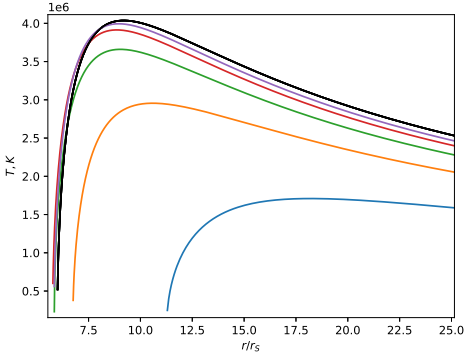


**Figure 8.** Case  $V = 0$ . The temperature distribution  $T(r)$  of a disk around a static black hole with mass accretion rate  $\dot{M} = 4.72 \times 10^{18} g/s$  and mass  $M = 14.8M_{\odot}$  for different values of  $\phi_0$  and fixed  $u_0 = 5.12 \times 10^{-7}$  as functions of the normalized radial coordinate  $r/r_s$ . The black curve corresponds to the Schwarzschild black hole. The initial value of scalar field is taken to be:  $\phi_0 = 0.5$  (blue curve),  $\phi_0 = 1$  (orange curve),  $\phi_0 = 2$  (green curve),  $\phi_0 = 4$  (red curve),  $\phi_0 = 8$  (purple curve).

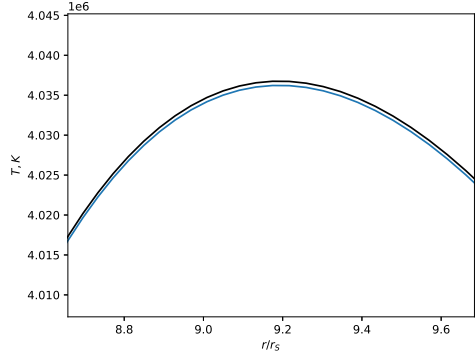


**Figure 9.** Case  $V = 0$ . The temperature distribution  $T(r)$  of a disk around a static black hole with mass accretion rate  $\dot{M} = 4.72 \times 10^{18} g/s$  and mass  $M = 14.8M_{\odot}$  for values of  $\phi_0 = 4 \times 10^{-5}$  and  $u_0 = 2.2 \times 10^{-17}$  as functions of the normalized radial coordinate  $r/r_s$ . The black curve corresponds to the Schwarzschild black hole.

the accretion characteristics for such a black hole.

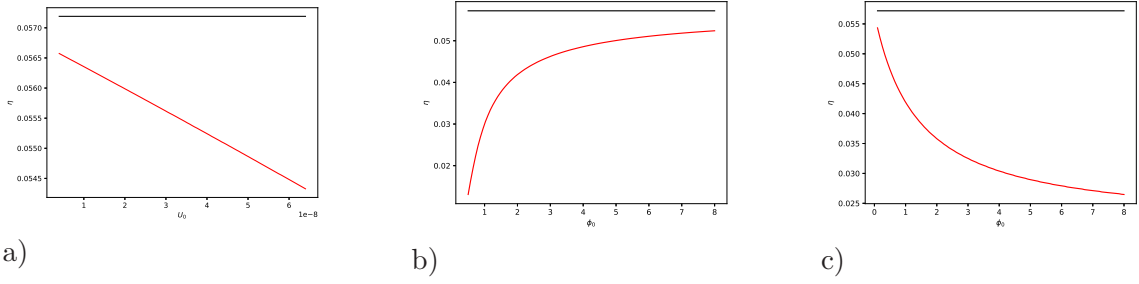


**Figure 10.** Case  $V = 0$ . The black curve corresponds to the Schwarzschild black hole. a). The efficiency for thin accretion disk around static black hole for different values of  $u_0$  and fixed  $\phi_0 = 1$  as functions of  $u_0$ . b). The efficiency for thin accretion disk around static black hole for different values of  $\phi_0$  and fixed  $u_0 = 5.12 \times 10^{-7}$  as functions of  $\phi_0$ . c). The efficiency for thin accretion disk around static black hole as functions of  $\phi_0$ . Connection between  $\phi_0$  and  $u_0$  is taken into account.

#### 5.1.4 Efficiency.

The discussion of efficiency deserves special attention.

1. The case of fixed  $\phi_0$  is shown in Figure (10a). As  $u_0$  increases, the efficiency decreases.
2. with the growth of  $\phi_0$  the efficiency increases and its value approaches the Schwarzschild one. Moreover, small values of  $\phi_0 < 1$  may differ by more than 80% from the predictions of GR (Figure (10b)).
3. If we take into account the relationship between  $u_0$  and  $\phi_0$  (5.1), we can see that as  $\phi_0$  increases, the efficiency decreases. This dependence is illustrated in Figure (10c). The difference with the maximum value is almost 50%. On the other hand, we can observe that no value of  $\phi_0$  achieves the efficiency value for a Schwarzschild black hole. We assume that it is a consequence of the fact that hybrid f(R)-gravity in its scalar-tensor form does not have a direct transition to GR for any  $\phi_0$ .

#### 5.2 Case $V = -\frac{\mu^2}{2}\phi^2 + \frac{\zeta}{4}\phi^4$

In the article [39] authors consider the only one case with the potential, and this potential has a Higgs-type form:

$$V = -\frac{\mu^2}{2}\phi^2 + \frac{\zeta}{4}\phi^4, \quad (5.2)$$

where  $\mu^2$  and  $\zeta$  are constants. We also focus on this case and obtain the picture of accretion. The Higgs potential is the most widely used in particle physics. Now we redefine constants  $\mu^2$  and  $\zeta$  into a dimensionless form as [39]

$$v(\phi) = \alpha\phi^2 + \beta\phi^4, \quad (5.3)$$

where

$$\alpha = -\frac{1}{4}\left(\frac{2GnM_{BH}}{c^2}\right)^2\mu^2, \quad \beta = \frac{1}{2}\left(\frac{2GnM_{BH}}{c^2}\right)^2\zeta^2. \quad (5.4)$$

The Higgs-type potential yields four-parameter  $(\alpha, \beta, \phi_0, u_0)$  solutions of the static gravitational field equations in hybrid f(R)-gravity. Authors of the article [39] restrict their analysis to investigating the role of constants  $\alpha$  and  $\beta$ , while keeping  $\phi_0$  and  $u_0$  fixed, and varying numerical values of  $\alpha$  and  $\beta$ . However, we consider a wider range of cases:

1. We fix  $u_0 = 10^{-8}$ ,  $\phi_0 = 1$ ,  $\beta = 10^{-10}$ , and take the range of  $\alpha = [-10^{-6}; -4 \times 10^{-5}]$ .
2. We fix  $u_0 = 10^{-8}$ ,  $\phi_0 = 1$ ,  $\alpha = -10^{-10}$ , and vary  $\beta = [2 \times 10^{-10}; 14 \times 10^{-10}]$ .
3. We study the case based on the Solar system data. We assume that the scalar field mass is defined as [26, 32]

$$m_\phi^2 = [2V_0 - V_\phi - (1 + \phi)\phi V_{\phi\phi}]/3|_{\phi=\phi_0}, \quad (5.5)$$

where subscript  $\phi$  denotes the derivative with respect to the scalar field. Subsequently,  $m_\phi^2$  has a connection with  $\alpha$  and  $\beta$  parameters:

$$m_\phi^2 = [-4/3\alpha\phi_0 - 16/3\beta\phi_0^3 - 10/3\beta\phi_0^4] \times 2 \left( \frac{c^2}{2GM_{BH}} \right)^2. \quad (5.6)$$

We save the connection between  $u_0$  and  $\phi_0$ , which is known from PPN analysis as derivative of  $\varphi = \frac{-2GM\phi_0 e^{-m_\phi r}}{3c^2 r}$  with respect to  $r$ . As a result, we get

$$u_0 = -\frac{2GM\phi_0 e^{-m_\phi r} m_\phi}{3c^2 r} - \frac{2GM\phi_0 e^{-m_\phi r}}{3c^2 r^2}. \quad (5.7)$$

In this case, we vary  $\alpha = [-10^{-6}; -4 \times 10^{-5}]$  and fix  $\beta = 10^{-20}$ ,  $\phi_0 = 4 \times 10^{-5}$ .

4. We assume  $m_\phi^2 = -\mu^2$  by analogy with quantum field theoretical models. We choose the following set of parameters:  $\alpha = [-10^{-6}; -4 \times 10^{-5}]$ ,  $\beta = 10^{-11}$ ,  $\phi_0 = 4 \times 10^{-5}$ .
5. We also consider the case of large values of  $\phi_0 = [0.1; 4]$  and fix  $\alpha = -10^{-10}$ ,  $\beta = 10^{-11}$ ,  $m_\phi^2 = -\mu^2$ .

The first two cases are inspired by the work [39]. However, we slightly extend the range of  $\alpha$  and  $\beta$  parameters to better illustrate changes in accretion characteristics. The third case is based on post-Newtonian analysis, relationships and constraints obtained from the solar system. This case seems to us the closest to reality in terms of the obtained characteristics. The fourth and fifth instances include the connection  $m_\phi^2 = -\mu^2$  that emerges from quantum field theoretical models, where  $-\mu^2$  signifies the scalar field particle mass. By extension, we give the same meaning to this quantity in hybrid f(R)-gravity. Data from accelerator experiments suggest that the Higgs self-coupling constant  $\zeta \approx 1/8$  for strong interactions. Nevertheless, the characteristics of the self-action of a scalar field in hybrid f(R)-gravity can differ markedly from those of Higgs bosons.

Further each of these cases is used to determine the characteristics of the accretion disk.

### 5.2.1 Energy flux

1. This case is illustrated in Figure (11). We can observe that as the modulus  $\alpha$  increases, the energy flux maximum also increases. Notably, at  $\alpha = -10^{-5}$ , it exceeds the Schwarzschild result. The maximum deviation for curves both above and below the Schwarzschild one is 0.95% and 0.47%, respectively.
2. When we vary the  $\beta$  parameter, no curve exceeds the Schwarzschild result. Furthermore, as  $\beta$  increases, the maximum of the energy flux decreases. This result is displayed in Figure (12).

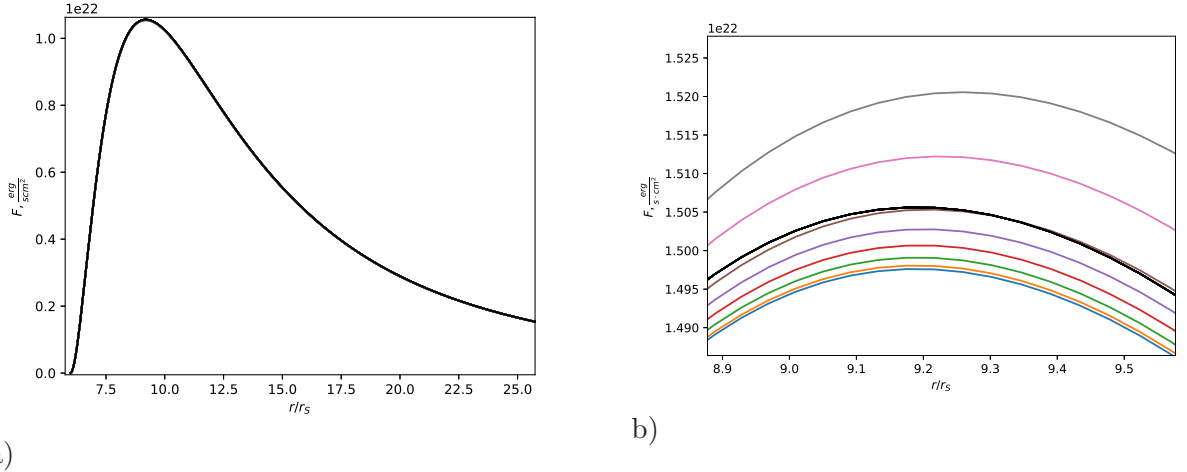


**Figure 11.** Hyggs-type potential case. The energy flux  $F(r)$  of a disk around a static black hole with mass accretion rate  $\dot{M} = 4.72 \times 10^{18} g/s$  and mass  $M = 14.8 M_{\odot}$  for different values of  $\alpha$  and fixed  $\phi_0 = 1$ ,  $u_0 = 10^{-8}$ ,  $\beta = 10^{-10}$  as functions of the normalized radial coordinate  $r/r_s$ . The black curve corresponds to the Schwarzschild black hole. The parameter  $\alpha$  is taken to be:  $\alpha = -4 \times 10^{-5}$  (grey curve),  $\alpha = -3 \times 10^{-5}$  (pink curve),  $\alpha = -2.1 \times 10^{-5}$  (brown curve),  $\alpha = -1.7 \times 10^{-5}$  (purple curve),  $\alpha = -1.3 \times 10^{-5}$  (red curve),  $\alpha = -9 \times 10^{-6}$  (green curve),  $\alpha = -5 \times 10^{-6}$  (orange curve),  $\alpha = -10^{-6}$  (blue curve). The figure on the right panel is a zoom version of the left one.

3. As shown in Figure (13) the energy flux maximum increases with the growth of the modulus  $\alpha$ . However, the change in the  $\beta$  parameter, while  $\alpha$  remains fixed, does not affect the position of the curve. This is due to the fact that  $\beta$  is multiplied by greater powers of  $\phi_0$  than  $\alpha$ , which means that its contribution is suppressed.
4. As in previous cases, with increasing modulus  $\alpha$ , an increase in the energy flux maximum is observed (see Figure (14)). However, in none of the cases is there an excess of the Schwarzschild curve. The maximum deviation from the Schwarzschild curve in this case is 0.01%. Similar to the previous case, changing  $\beta$  with a fixed  $\alpha$  does not contribute to the shift of the energy flux curve.
5. As  $\phi_0$  increases, the maximum value of the energy flux decreases. The maximum deviation is 80% from the Schwarzschild curve. This case is illustrated in Figure (15).

### 5.2.2 Emission spectra.

In this subsection we present the spectral energy distribution of the disk radiation around the black holes for the general relativistic case, and for the hybrid metric-Palatini f(R)-gravity.

1. In Figure (16), we vary  $\alpha$  while fixing other parameters. The luminosity maximum exceeds Schwarzschild predictions at  $\alpha = -1.5 \times 10^{-5}$ . Thus, the luminosity changes faster than the energy flux when we vary the  $\alpha$  parameter.
2. With a fixed  $\alpha$  parameter and varying  $\beta$  parameter, we see the same pattern as for the energy flux: with increasing  $\beta$ , the luminosity decreases (see Figure (17)).

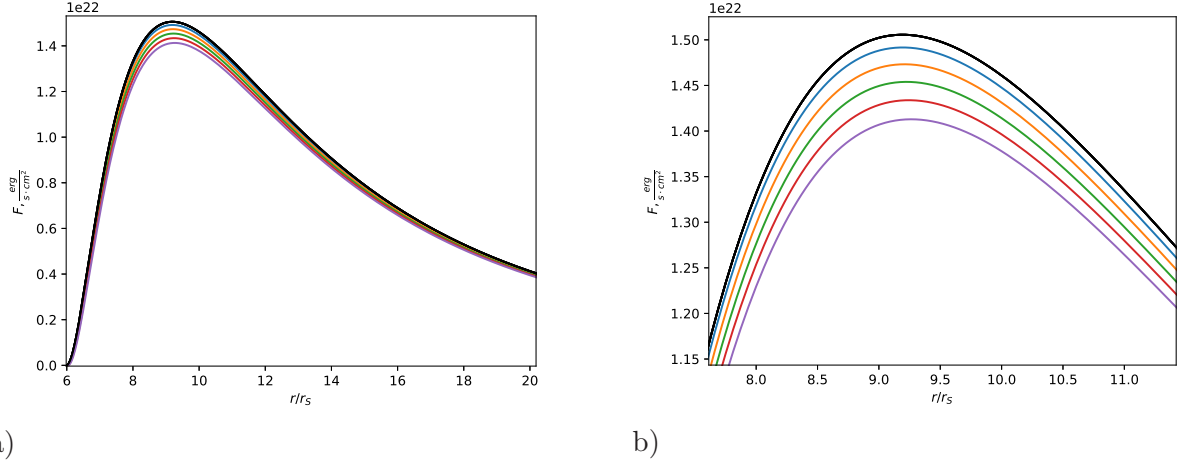


**Figure 12.** Hyggs-type potential case. The energy flux  $F(r)$  of a disk around a static black hole with mass accretion rate  $\dot{M} = 4.72 \times 10^{18} g/s$  and mass  $M = 14.8 M_\odot$  for different values of  $\beta$  and fixed  $\phi_0 = 1$ ,  $u_0 = 10^{-8}$ ,  $\alpha = -10^{-10}$  as functions of the normalized radial coordinate  $r/r_s$ . The black curve corresponds to the Schwarzschild black hole. The parameter  $\beta$  is taken to be:  $\beta = 2 \times 10^{-10}$  (blue curve),  $\beta = 5 \times 10^{-10}$  (orange curve),  $\beta = 8 \times 10^{-10}$  (green curve),  $\beta = 1.1 \times 10^{-9}$  (red curve),  $\beta = 1.4 \times 10^{-9}$  (purple curve). The figure on the right panel is a zoom version of the left one.

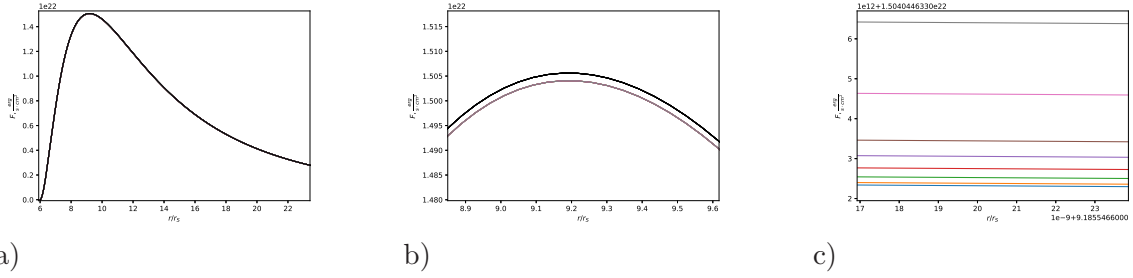


**Figure 13.** Hyggs-type potential case. The energy flux  $F(r)$  of a disk around a static black hole with mass accretion rate  $\dot{M} = 4.72 \times 10^{18} g/s$  and mass  $M = 14.8 M_\odot$  for different values of  $\alpha$  and fixed  $\phi_0 = 4 \times 10^{-5}$ ,  $\beta = 10^{-20}$  as functions of the normalized radial coordinate  $r/r_s$ . The connections (5.6) and (5.7) are taken into account. b) The black curve corresponds to the Schwarzschild black hole, the brown curve corresponds different parameters  $\alpha$ . c) Zoom version. The parameter  $\alpha$  is taken to be:  $\alpha = -4 \times 10^{-5}$  (grey curve),  $\alpha = -3 \times 10^{-5}$  (pink curve),  $\alpha = -2.1 \times 10^{-5}$  (brown curve),  $\alpha = -1.7 \times 10^{-5}$  (purple curve),  $\alpha = -1.3 \times 10^{-5}$  (red curve),  $\alpha = -9 \times 10^{-6}$  (green curve),  $\alpha = -5 \times 10^{-6}$  (orange curve),  $\alpha = -10^{-6}$  (blue curve).

3. Taking into account the connection between the mass of the scalar field  $m_\phi$  and the parameters  $\alpha$  and  $\beta$ , the picture does not differ from the energy flux. As the modulus  $\alpha$  grows, the luminosity maximum increases. Changes in the  $\beta$  parameter with a fixed  $\alpha$  do not affect the position of the curve. This case is illustrated in Figure (18).
4. In Figure (19), we can see that the connection between mass of the scalar field and the parameter of potential  $m_\phi^2 = -\mu^2$  yields an increase in luminosity as the modulus of  $\alpha$  increases. Varying the  $\beta$  parameter in this case also has no effect.
5. As  $\phi$  varies, the largest values of  $\phi$  produce the greatest deviation from the Schwarzschild



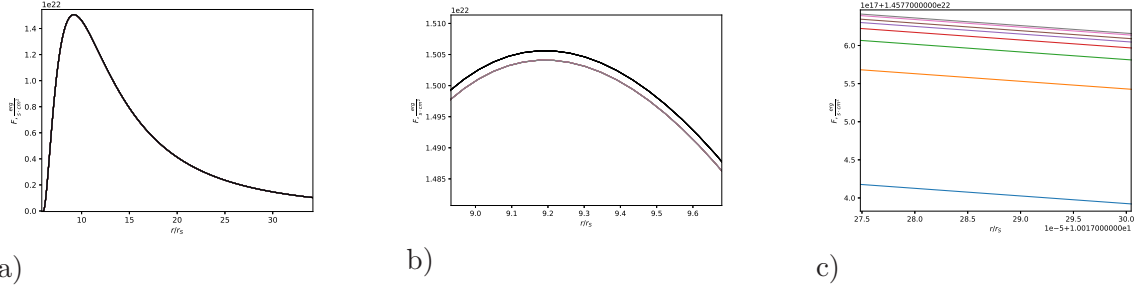


**Figure 14.** Hyggs-type potential case. The energy flux  $F(r)$  of a disk around a static black hole with mass accretion rate  $\dot{M} = 4.72 \times 10^{18} g/s$  and mass  $M = 14.8M_{\odot}$  for different values of  $\alpha$  and fixed  $\phi_0 = 4 \times 10^{-5}$ ,  $\beta = 10^{-11}$  as functions of the normalized radial coordinate  $r/r_s$ . The connection  $m_{\varphi}^2 = -\mu^2$  is taken into account. b) The black curve corresponds to the Schwarzschild black hole, the brown curve corresponds different parameters  $\alpha$ . c) Zoom version. The parameter  $\alpha$  is taken to be:  $\alpha = -4 \times 10^{-5}$  (grey curve),  $\alpha = -3 \times 10^{-5}$  (pink curve),  $\alpha = -2.1 \times 10^{-5}$  (brown curve),  $\alpha = -1.7 \times 10^{-5}$  (purple curve),  $\alpha = -1.3 \times 10^{-5}$  (red curve),  $\alpha = -9 \times 10^{-6}$  (green curve),  $\alpha = -5 \times 10^{-6}$  (orange curve),  $\alpha = -10^{-6}$  (blue curve).

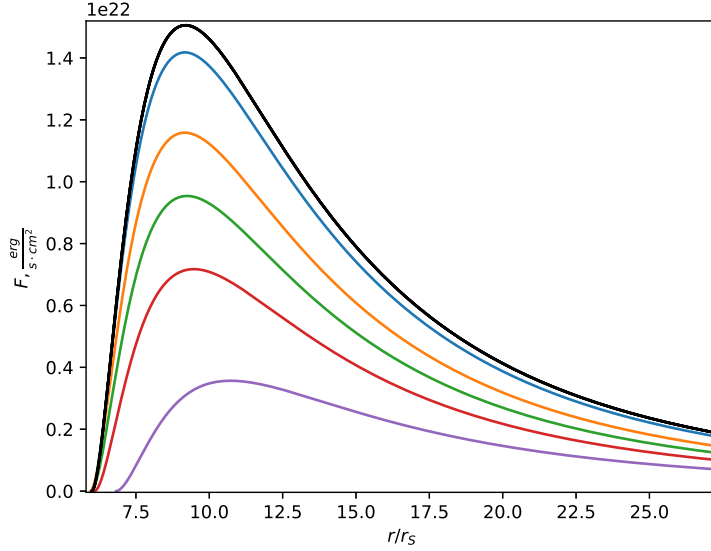
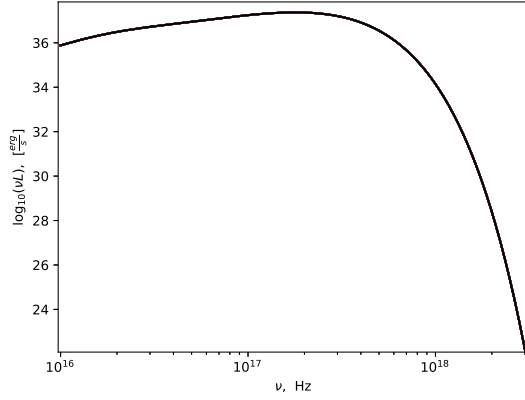
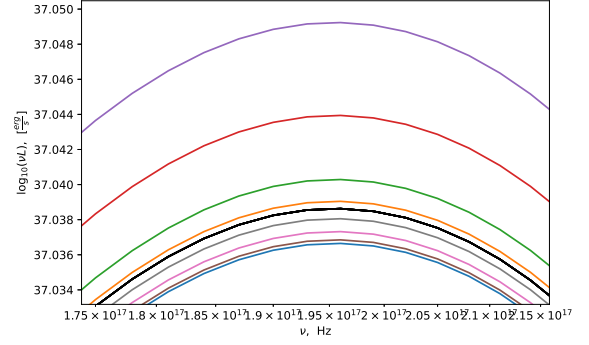


**Figure 15.** Hyggs-type potential case. The energy flux  $F(r)$  of a disk around a static black hole with mass accretion rate  $\dot{M} = 4.72 \times 10^{18} g/s$  and mass  $M = 14.8M_{\odot}$  for different values of  $\phi_0$  and fixed  $\alpha = -10^{-10}$ ,  $\beta = 10^{-11}$  as functions of the normalized radial coordinate  $r/r_s$ . The connection  $m_{\varphi}^2 = -\mu^2$  is taken into account. The black curve corresponds to the Schwarzschild black hole. The initial value of scalar field is taken to be:  $\phi_0 = 0.1$  (blue curve),  $\phi_0 = 0.5$  (orange curve),  $\phi_0 = 1$  (green curve),  $\phi_0 = 2$  (red curve),  $\phi_0 = 4$  (purple curve).

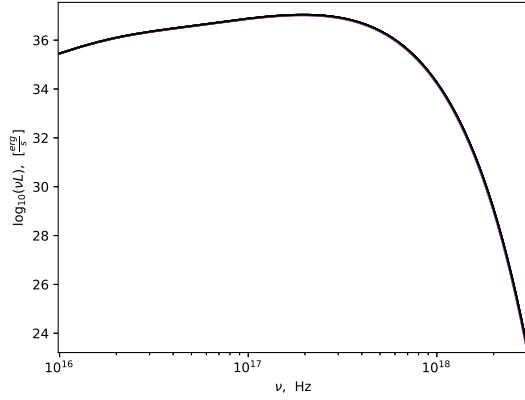


a)

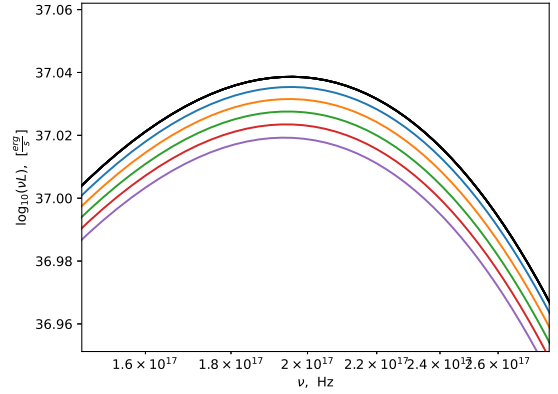


b)

**Figure 16.** Hyggs-type potential case. The emission spectrum  $\nu L(\nu)$  of the accretion disk around a static black hole with mass accretion rate  $\dot{M} = 4.72 \times 10^{18} g/s$  and mass  $M = 14.8 M_{\odot}$  for different values of  $\alpha$  and fixed  $\phi_0 = 1$ ,  $u_0 = 10^{-8}$ ,  $\beta = 10^{-10}$  as functions of frequency  $\nu$ . The black curve corresponds to the Schwarzschild black hole. The parameter  $\alpha$  is taken to be:  $\alpha = -4 \times 10^{-5}$  (purple curve),  $\alpha = -3 \times 10^{-5}$  (red curve),  $\alpha = -2.1 \times 10^{-5}$  (green curve),  $\alpha = -1.7 \times 10^{-5}$  (orange curve),  $\alpha = -1.3 \times 10^{-5}$  (grey curve),  $\alpha = -9 \times 10^{-6}$  (pink curve),  $\alpha = -5 \times 10^{-6}$  (brown curve),  $\alpha = -10^{-6}$  (blue curve). The figure on the right panel is a zoom version of the left one.



a)



b)

**Figure 17.** Hyggs-type potential case. The emission spectrum  $\nu L(\nu)$  of the accretion disk around a static black hole with mass accretion rate  $\dot{M} = 4.72 \times 10^{18} g/s$  and mass  $M = 14.8 M_{\odot}$  for different values of  $\beta$  and fixed  $\phi_0 = 1$ ,  $u_0 = 10^{-8}$ ,  $\alpha = -10^{-10}$  as functions of frequency  $\nu$ . The black curve corresponds to the Schwarzschild black hole. The parameter  $\beta$  is taken to be:  $\beta = 2 \times 10^{-10}$  (blue curve),  $\beta = 5 \times 10^{-10}$  (orange curve),  $\beta = 8 \times 10^{-10}$  (green curve),  $\beta = 1.1 \times 10^{-9}$  (red curve),  $\beta = 1.4 \times 10^{-9}$  (purple curve). The figure on the right panel is a zoom version of the left one.

curve. However, in this case, the maximum deviation from the Schwarzschild curve is only 3% (see Figure (20)).

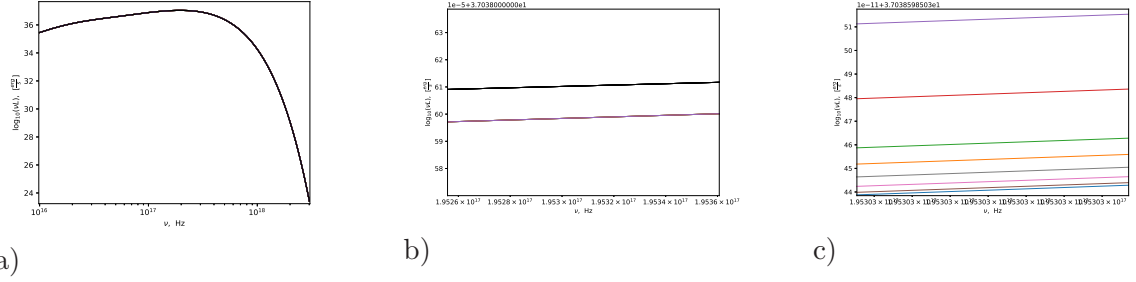


**Figure 18.** Hyggs-type potential case. The emission spectrum  $\nu L(\nu)$  of the accretion disk around a static black hole with mass accretion rate  $\dot{M} = 4.72 \times 10^{18} g/s$  and mass  $M = 14.8M_{\odot}$  for different values of  $\alpha$  and fixed  $\phi_0 = 4 \times 10^{-5}$ ,  $\beta = 10^{-20}$  as functions of frequency  $\nu$ . The connections (5.6) and (5.7) are taken into account. b) The black curve corresponds to the Schwarzschild black hole, the brown curve corresponds different parameters  $\alpha$ . c) Zoom version. The parameter  $\alpha$  is taken to be  $\alpha = -4 \times 10^{-5}$  (purple curve),  $\alpha = -3 \times 10^{-5}$  (red curve),  $\alpha = -2.1 \times 10^{-5}$  (green curve),  $\alpha = -1.7 \times 10^{-5}$  (orange curve),  $\alpha = -1.3 \times 10^{-5}$  (grey curve),  $\alpha = -9 \times 10^{-6}$  (pink curve),  $\alpha = -5 \times 10^{-6}$  (brown curve),  $\alpha = -10^{-6}$  (blue curve).

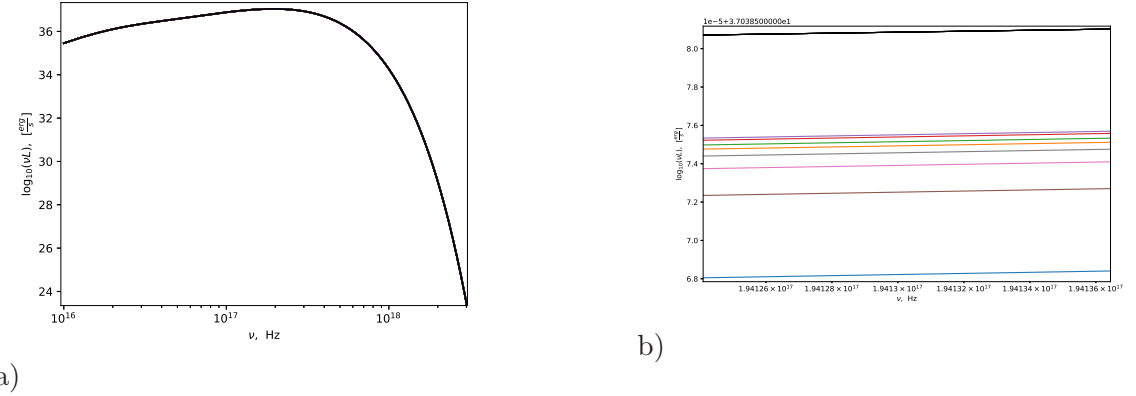


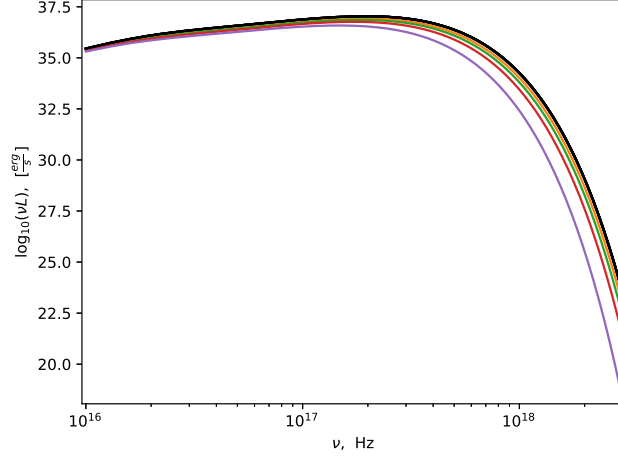
**Figure 19.** Hyggs-type potential case. The emission spectrum  $\nu L(\nu)$  of the accretion disk around a static black hole with mass accretion rate  $\dot{M} = 4.72 \times 10^{18} g/s$  and mass  $M = 14.8M_{\odot}$  for different values of  $\alpha$  and fixed  $\phi_0 = 4 \times 10^{-5}$ ,  $\beta = 10^{-11}$  as functions of frequency  $\nu$ . The connection  $m_{\varphi}^2 = -\mu^2$  is taken into account. b) Zoom version. The parameter  $\alpha$  is taken to be:  $\alpha = -4 \times 10^{-5}$  (purple curve),  $\alpha = -3 \times 10^{-5}$  (red curve),  $\alpha = -2.1 \times 10^{-5}$  (green curve),  $\alpha = -1.7 \times 10^{-5}$  (orange curve),  $\alpha = -1.3 \times 10^{-5}$  (grey curve),  $\alpha = -9 \times 10^{-6}$  (pink curve),  $\alpha = -5 \times 10^{-6}$  (brown curve),  $\alpha = -10^{-6}$  (blue curve). The black curve corresponds to the Schwarzschild black hole.

### 5.2.3 Temperature.

Temperature is related to energy flux through Stefan-Boltzmann equation. As in the case without potential, all conclusions that are true for the energy flux are also true for the effective temperature.

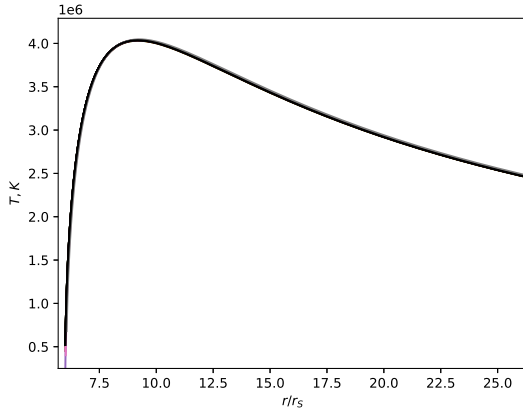
### 5.2.4 Efficiency.

For all previously considered cases, we also evaluated the effect of changing various parameters on the efficiency (see Figure (26)).

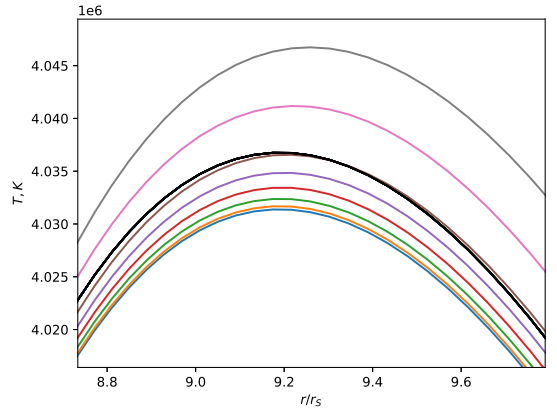


c)

**Figure 20.** Hyggs-type potential case. The emission spectrum  $\nu L(\nu)$  of the accretion disk around a static black hole with mass accretion rate  $\dot{M} = 4.72 \times 10^{18} g/s$  and mass  $M = 14.8 M_\odot$  for different values of  $\phi_0$  and fixed  $\alpha = -10^{-10}$ ,  $\beta = 10^{-11}$  as functions of frequency  $\nu$ . The connection  $m_\phi^2 = -\mu^2$  is taken into account. The black curve corresponds to the Schwarzschild black hole. The initial value of scalar field is taken to be:  $\phi_0 = 0.1$  (blue curve),  $\phi_0 = 0.5$  (orange curve),  $\phi_0 = 1$  (green curve),  $\phi_0 = 2$  (red curve),  $\phi_0 = 4$  (purple curve).



a)



b)

**Figure 21.** Hyggs-type potential case. The temperature distribution  $T(r)$  of a disk around a static black hole with mass accretion rate  $\dot{M} = 4.72 \times 10^{18} g/s$  and mass  $M = 14.8 M_\odot$  for different values of  $\alpha$  and fixed  $\phi_0 = 1$ ,  $u_0 = 10^{-8}$ ,  $\beta = 10^{-10}$  as functions of the normalized radial coordinate  $r/r_s$ . The black curve corresponds to the Schwarzschild black hole. The parameter  $\alpha$  is taken to be:  $\alpha = -4 \times 10^{-5}$  (grey curve),  $\alpha = -3 \times 10^{-5}$  (pink curve),  $\alpha = -2.1 \times 10^{-5}$  (brown curve),  $\alpha = -1.7 \times 10^{-5}$  (purple curve),  $\alpha = -1.3 \times 10^{-5}$  (red curve),  $\alpha = -9 \times 10^{-6}$  (green curve),  $\alpha = -5 \times 10^{-6}$  (orange curve),  $\alpha = -10^{-6}$  (blue curve). The figure on the right panel is a zoom version of the left one.

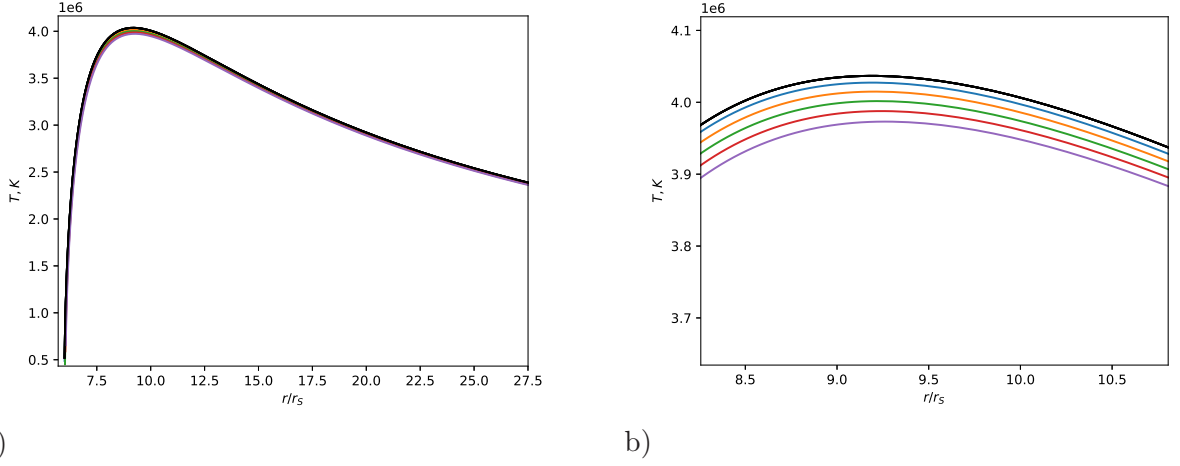


**Figure 22.** Hyggs-type potential case. The temperature distribution  $T(r)$  of a disk around a static black hole with mass accretion rate  $\dot{M} = 4.72 \times 10^{18} g/s$  and mass  $M = 14.8 M_{\odot}$  for different values of  $\beta$  and fixed  $\phi_0 = 1$ ,  $u_0 = 10^{-8}$ ,  $\alpha = -10^{-10}$  as functions of the normalized radial coordinate  $r/r_s$ . The black curve corresponds to the Schwarzschild black hole. The parameter  $\beta$  is taken to be:  $\beta = 2 \times 10^{-10}$  (blue curve),  $\beta = 5 \times 10^{-10}$  (orange curve),  $\beta = 8 \times 10^{-10}$  (green curve),  $\beta = 1.1 \times 10^{-9}$  (red curve),  $\beta = 1.4 \times 10^{-9}$  (purple curve). The figure on the right panel is a zoom version of the left one.

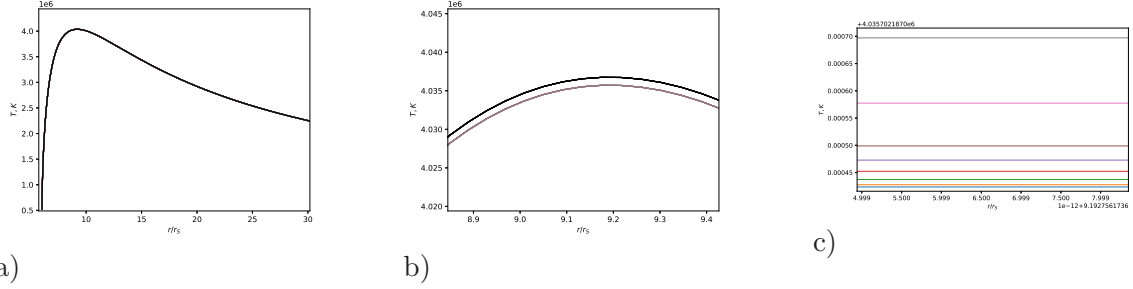


**Figure 23.** Hyggs-type potential case. The temperature distribution  $T(r)$  of a disk around a static black hole with mass accretion rate  $\dot{M} = 4.72 \times 10^{18} g/s$  and mass  $M = 14.8 M_{\odot}$  for different values of  $\alpha$  and fixed  $\phi_0 = 4 \times 10^{-5}$ ,  $\beta = 10^{-20}$  as functions of the normalized radial coordinate  $r/r_s$ . The connections (5.6) and (5.7) are taken into account. b) The black curve corresponds to the Schwarzschild black hole, the brown curve corresponds different parameters  $\alpha$ . c) Zoom version. The parameter  $\alpha$  is taken to be:  $\alpha = -4 \times 10^{-5}$  (grey curve),  $\alpha = -3 \times 10^{-5}$  (pink curve),  $\alpha = -2.1 \times 10^{-5}$  (brown curve),  $\alpha = -1.7 \times 10^{-5}$  (purple curve),  $\alpha = -1.3 \times 10^{-5}$  (red curve),  $\alpha = -9 \times 10^{-6}$  (green curve),  $\alpha = -5 \times 10^{-6}$  (orange curve),  $\alpha = -10^{-6}$  (blue curve).

1. As the modulus of  $\alpha$  increases, the efficiency also increases. At values of  $\alpha < -3.5 \times 10^{-5}$ , the efficiency exceeds the Schwarzschild predictions.
2. With an increase in  $\beta$  and a fixed  $\alpha$ , a decrease in efficiency is observed. Moreover, the Schwarzschild value cannot be achieved for any value of  $\beta$  in this case.
3. In this case, neither when changing  $\alpha$  nor when changing  $\beta$  are there any changes in the efficiency value. It remains constant and is 98% of the value predicted by Schwarzschild solution.

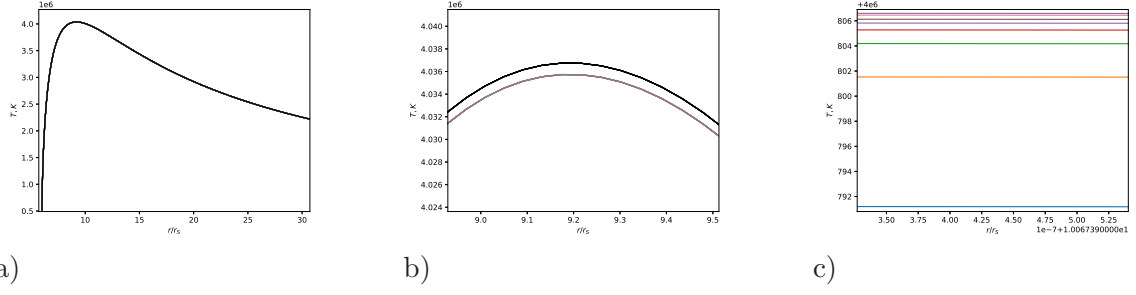


**Figure 24.** Hyggs-type potential case. The temperature distribution  $T(r)$  of a disk around a static black hole with mass accretion rate  $\dot{M} = 4.72 \times 10^{18} g/s$  and mass  $M = 14.8 M_{\odot}$  for different values of  $\alpha$  and fixed  $\phi_0 = 4 \times 10^{-5}$ ,  $\beta = 10^{-11}$  as functions of the normalized radial coordinate  $r/r_s$ . The connection  $m_{\varphi}^2 = -\mu^2$  is taken into account. b) The black curve corresponds to the Schwarzschild black hole, the brown curve corresponds to different parameters  $\alpha$ . c) Zoom version. The parameter  $\alpha$  is taken to be:  $\alpha = -4 \times 10^{-5}$  (grey curve),  $\alpha = -3 \times 10^{-5}$  (pink curve),  $\alpha = -2.1 \times 10^{-5}$  (brown curve),  $\alpha = -1.7 \times 10^{-5}$  (purple curve),  $\alpha = -1.3 \times 10^{-5}$  (red curve),  $\alpha = -9 \times 10^{-6}$  (green curve),  $\alpha = -5 \times 10^{-6}$  (orange curve),  $\alpha = -10^{-6}$  (blue curve).

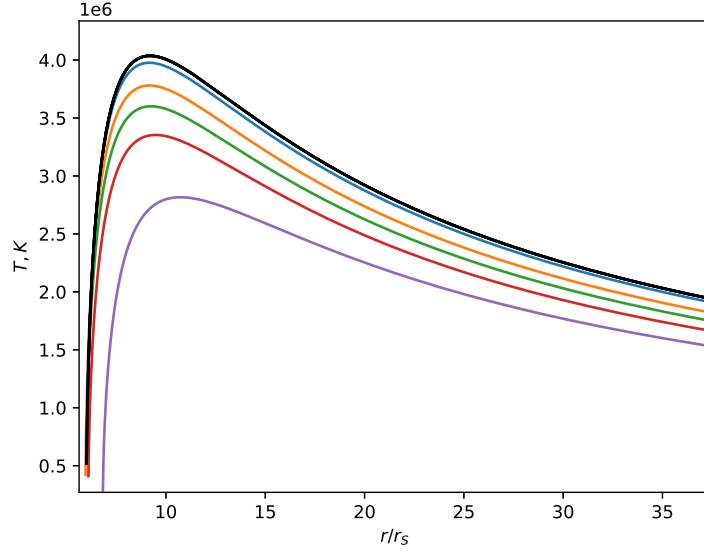


**Figure 25.** Hyggs-type potential case. The temperature distribution  $T(r)$  of a disk around a static black hole with mass accretion rate  $\dot{M} = 4.72 \times 10^{18} g/s$  and mass  $M = 14.8 M_{\odot}$  for different values of  $\phi_0$  and fixed  $\alpha = -10^{-10}$ ,  $\beta = 10^{-11}$  as functions of the normalized radial coordinate  $r/r_s$ . The connection  $m_{\varphi}^2 = -\mu^2$  is taken into account. The black curve corresponds to the Schwarzschild black hole. The initial value of scalar field is taken to be:  $\phi_0 = 0.1$  (blue curve),  $\phi_0 = 0.5$  (orange curve),  $\phi_0 = 1$  (green curve),  $\phi_0 = 2$  (red curve),  $\phi_0 = 4$  (purple curve).

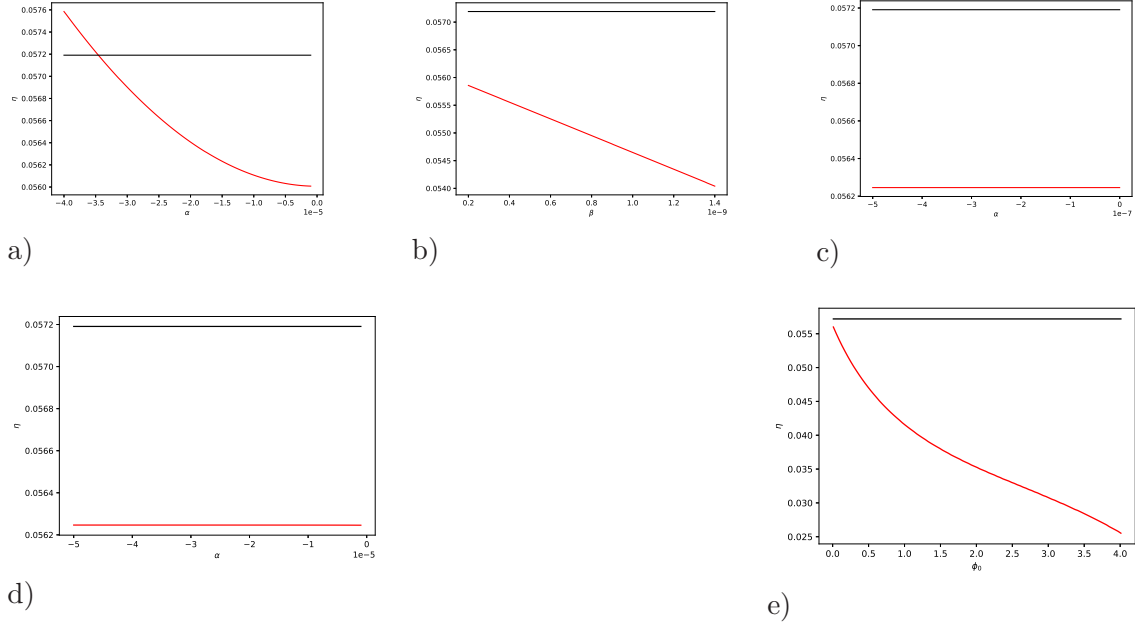


**Figure 26.** Hyggs-type potential case. The black curve corresponds to the Schwarzschild black hole in all figures. The efficiency for thin accretion disk around static black hole a) for different values of  $\alpha$  and fixed  $\phi_0 = 1$ ,  $u_0 = 10^{-8}$ ,  $\beta = 10^{-10}$ ; b) for different values of  $\beta$  and fixed  $\phi_0 = 1$ ,  $u_0 = 10^{-8}$ ,  $\alpha = -10^{-10}$ ; c) for different values of  $\alpha$  and fixed  $\phi_0 = 4 \times 10^{-5}$ ,  $\beta = 10^{-20}$ . The connections (5.6) and (5.7) are taken into account; d) for different values of  $\alpha$  and fixed  $\phi_0 = 4 \times 10^{-5}$ ,  $\beta = 10^{-11}$ . The connection  $m_\varphi^2 = -\mu^2$  is taken into account; e) for different values of  $\phi_0$  and fixed  $\alpha = -10^{-10}$ ,  $\beta = 10^{-11}$ . The connection  $m_\varphi^2 = -\mu^2$  is taken into account.

4. In the case of  $m_\phi = -\mu$ , we obtain the same result as in the previous one.
5. However, when considering large values of  $\phi_0 > 1$  and taking into account  $m_\phi = -\mu$ , we observe a significant decrease in efficiency, which can be less than 40% of the Schwarzschild prediction.

## 6 Discussion

In this paper, the properties of thin accretion disks around black holes in hybrid metric-Palatini  $f(R)$ -gravity are investigated. As a foundation for our research, we use the numerical solution for a static spherical symmetric black hole obtained in the article [39]. To study accretion properties, the steady-state Novikov-Thorne model is employed. In this paper, we consider two types of solutions: first, we study a solution without a potential  $V = 0$ , and then we take a Higgs-type potential  $V = -\frac{\mu^2}{2}\phi^2 + \frac{\zeta}{4}\phi^4$ . As characteristics of the accretion disk, we numerically obtain the energy flux, temperature distribution and the emission spectra. The numerical black hole solution, which is derived in the article [39], has a certain set of free parameters. This set is determined, among other things, by the presence of the potential. In the case without a potential  $V = 0$ , these parameters include the initial value of the scalar field  $\phi_0$  and its derivative  $u_0$ . In the case with a Hyggs-type potential there are two additional parameters:  $\alpha$  and  $\beta$ .

In the case  $V = 0$ , we find the following features of the accretion disks in the hybrid f(R)-model. Results, which are close to Schwarzschild ones, can be obtained when we take sufficiently large values of  $\phi_0$  for large  $u_0$  or small values of  $u_0$  for small  $\phi_0$ . However, the former result seems unrealistic to us, since the scalar field should take its background value at a large distance from the black hole. This value is significantly less than unity [31], [32], [33]. Therefore,  $\phi_0 > 1$  looks unnatural.

Another approach to selecting the initial parameters  $\phi_0$  and  $u_0$  arises from post-Newtonian analysis. Far from the black hole, where we take the values of the free parameters, the gravitational field is weak, allowing us to consider the post-Newtonian expansion. Within the post-Newtonian analysis, the scalar field is considered as the sum of the background value and its perturbation  $\phi = \phi_0 + \varphi$ . The background value  $\phi_0$  is a constant quantity, unlike the perturbation  $\varphi$ . Thus, taking the derivative of the scalar field  $\phi$  with respect to the distance at infinity, we simply obtain the value of  $u_0$ . As a result, we derive the connection eq. (5.1) between  $u_0$  and  $\phi_0$ . If such a connection is established and the values of  $\phi_0$  are taken within the limits set by the Cassini experiment [53], then we obtain the curves for the energy flux, temperature distribution and the emission spectra that practically do not deviate from the Schwarzschild results (see Figures (3), (6)). In this case,  $u_0$  takes a small values ( $\sim 10^{-11}$ ), which once again speaks in favor of choosing small values of the initial parameters due to their naturalness.

In the case of a Higgs-type potential, the theory includes four free parameters:  $u_0$ ,  $\phi_0$ ,  $\alpha$  and  $\beta$ . Parameters  $\alpha$  and  $\beta$  are woven into the structure of the potential itself. At first, we consider all parameters as independent quantities. A large modulus  $\alpha$  and sufficiently large  $\phi_0 > 1$  lead to a situation, where the maximum energy flux and the emission spectrum can exceeds the Schwarzschild prediction. This situation is unique and does not occur with any other combinations of parameters, leading us to conclude that large values of  $\phi_0$  are unrealistic. With an increase in the  $\beta$  parameter, a decrease in the energy flux maximum is observed, although not significant. No  $\beta$  parameter yields a curve that exceeds the Schwarzschild prediction.

Then, we once again consider a set of parameters based on the limitations obtained from experiments in the solar system. We also use the relationship between the parameters resulting from the post-Newtonian expansion. In this case, all parameters turn out to be small. With an increase in the modulus  $\alpha$ , a decrease in the maximum of energy flux is observed.

The last case is based on an analogy with particle physics. We assume that the mass of the scalar field  $m_\phi^2 = -\mu^2$ . The relationship (5.7) between  $\phi_0$ ,  $u_0$  and the mass of the scalar field  $m_\phi$  is preserved. In this case, it is found that even at large values of  $\alpha$ , the energy flux, temperature distribution and the emission spectra would still be less than Schwarzschild predictions. However, if the parameter  $\phi_0$  is increased, then at sufficiently large values of  $\phi_0$ , the energy flux, temperature distribution and the emission spectra begin to decrease significantly, and the difference can already exceed 80% at  $\phi_0 = 4$ .

Another important characteristic of the accretion process is the efficiency. This quantity demonstrates the ability of the central body to convert rest mass into outgoing radiation. In the case without potential, the efficiency values closest to the Schwarzschild prediction can be achieved when both  $u_0$  and  $\phi_0$  are taken to be either large or small. The most realistic result is obtained by taking into account the relationship (5.1) between  $\phi_0$  and  $u_0$ , and  $\phi_0$  is taken within the constraints imposed from the solar system. When we consider a model with a Hyggs-type potential, the results for efficiency are the same as for other accretion



characteristics. The only case where the efficiency exceeds the Schwarzschild prediction is when  $\alpha$ ,  $\phi_0$  and  $u_0$  are all large. An interesting situation is observed when we take small values of  $\phi_0$  and  $u_0$ . Regardless of the type of connection between these parameters, the efficiency becomes constant. At the same time, for any values of the parameters  $\alpha$  and  $\beta$ , it does not reach the Schwarzschild prediction if  $\phi_0$  is taken to be small. In the case of large values of  $\phi_0 > 1$  and the presence of a relationship (5.7) between the parameters, there is a significant deviation from Schwarzschild predictions.

## 7 Conclusions

Accretion disks in hybrid metric-Palatini  $f(R)$ -gravity around stellar static spherical symmetric black holes are colder and less luminous than in GR. We assume one main reason to these phenomena. The radius of the last stable circular orbit in hybrid  $f(R)$ -gravity is larger than in Schwarzschild case. Accretion disks become more luminous the closer they are to the black hole. Since the last stable orbit is farther from the black hole in hybrid  $f(R)$ -gravity, the contribution to the luminosity at high energies reduces. In turn, the effect of increasing the radius of the last stable orbit is due to the following fact. The gravitational field is stronger than in GR. Thus, the influence of the gravitational field of a black hole captures larger distances, which is the reason for the increase in the radius of the last stable orbit.

The temperature and luminosity excess relative to the values predicted by the Schwarzschild solution is observed only in one case: when considering a model with a Higgs-type potential, with large values of parameters  $\alpha$ ,  $\phi_0$  and  $u_0$ . However, such a set of parameters seems to be unrealistic as it is not consistent with the limitations imposed by other experiments on the background value of the scalar field (the value away from the black hole).

Another interesting consequence of this study is that in all cases, except aforementioned unrealistic one, the Schwarzschild values are not reached with any changes in the parameters. We believe that this is a consequence of the fact that hybrid  $f(R)$ -gravity does not have a direct transition to GR. Large values of  $\phi_0$ ,  $u_0$  and  $\alpha$  contradict this property of the theory.

In this paper, we consider the case of a static spherical symmetric black hole. Unfortunately, the probability that this type of black holes is realized in nature is extremely small. Therefore, to compare predictions of hybrid  $f(R)$ -gravity with observations, it is necessary to obtain a Kerr-type black-hole solution. This study will shed light on the realism of the theory and allow for constraints on free parameters of the hybrid  $f(R)$ -gravity, including through the study of accretion disks around rotating black holes. This is a subject for future research.

## Acknowledgments

The authors thank G. V. Lipunova for discussions and comments on the topics of this paper. P.I. Dyadina acknowledges support from RSF grant 22-72-00022.

## References

- [1] J.H. Oort, *The force exerted by the stellar system in the direction perpendicular to the galactic plane and some related problems*, *Bulletin of the Astronomical Institutes of the Netherlands* **6** (1932) 249.
- [2] F. Zwicky, *Die Rotverschiebung von extragalaktischen Nebeln*, *Helvetica Physica Acta* **6** (1933) 110.

- [3] S. Perlmutter, G. Aldering, G. Goldhaber, R.A. Knop, P. Nugent, P.G. Castro et al., *Measurements of  $\Omega$  and  $\Lambda$  from 42 high-redshift supernovae*, *Astrophys.J.* **517** (1999) 565 [[astro-ph/9812133](#)].
- [4] A.G. Riess, A.V. Filippenko, P. Challis, A. Clocchiatti, A. Diercks, P.M. Garnavich et al., *Observational evidence from supernovae for an accelerating universe and a cosmological constant*, *Astron.J.* **116** (1998) 1009 [[astro-ph/9805201](#)].
- [5] A.G. Riess, L.-G. Strolger, J. Tonry, S. Casertano, H.C. Ferguson, B. Mobasher et al., *Type Ia supernova discoveries at  $z > 1$  from the hubble space telescope: Evidence for past deceleration and constraints on dark energy evolution*, *The Astrophysical Journal* **607** (2004) 665.
- [6] A.G. Riess, P.E. Nugent, R.L. Gilliland, B.P. Schmidt, J. Tonry, M. Dickinson et al., *The farthest known supernova: Support for an accelerating universe and a glimpse of the epoch of deceleration*, *Astrophys.J.* **560** (2001) 49 [[astro-ph/0104455](#)].
- [7] S. Perlmutter, M.S. Turner and M. White, *Constraining dark energy with type Ia supernovae and large-scale structure*, *Phys.Rev.Lett.* **83** (1999) 670 [[astro-ph/9901052](#)].
- [8] A. Starobinsky, *A new type of isotropic cosmological models without singularity*, *Physics Letters B* **91** (1980) 99.
- [9] A.H. Guth, *Inflationary universe: A possible solution to the horizon and flatness problems*, *Physical Review D* **23** (1981) 347.
- [10] A. Linde, *A new inflationary universe scenario: A possible solution of the horizon, flatness, homogeneity, isotropy and primordial monopole problems*, *Physics Letters B* **108** (1982) 389.
- [11] P.G. Bergmann, *Comments on the scalar-tensor theory*, *International Journal of Theoretical Physics* **1** (1968) 25.
- [12] A.D. Felice and S. Tsujikawa,  *$f(r)$  theories*, *Living Reviews in Relativity* **13** (2010) .
- [13] S. Nojiri, S. Odintsov and V. Oikonomou, *Modified gravity theories on a nutshell: Inflation, bounce and late-time evolution*, *Physics Reports* **692** (2017) 1.
- [14] S. Nojiri and S.D. Odintsov, *Unified cosmic history in modified gravity: From  $f(r)$  theory to lorentz non-invariant models*, *Physics Reports* **505** (2011) 59.
- [15] T. Chiba,  *$1/r$  gravity and scalar-tensor gravity*, *Physics Letters B* **575** (2003) 1.
- [16] G.J. Olmo, *The gravity lagrangian according to solar system experiments*, *Physical Review Letters* **95** (2005) 261102.
- [17] G.J. Olmo, *Limit to general relativity in  $f(r)$  theories of gravity*, *Physical Review D* **75** (2007) 023511.
- [18] S. Nojiri and S.D. Odintsov, *Modified  $f(r)$  gravity unifying  $R^m$  inflation with the  $\Lambda$ CDM epoch*, *Phys. Rev. D* **77** (2008) 026007.
- [19] G. Cognola, E. Elizalde, S. Nojiri, S.D. Odintsov, L. Sebastiani and S. Zerbini, *Class of viable modified  $f(r)$  gravities describing inflation and the onset of accelerated expansion*, *Phys. Rev. D* **77** (2008) 046009.
- [20] S.D. Odintsov, D.S.-C. Gómez and G.S. Sharov, *Is exponential gravity a viable description for the whole cosmological history?*, *The European Physical Journal C* **77** (2017) .
- [21] S. Capozziello and M. Francaviglia, *Extended theories of gravity and their cosmological and astrophysical applications*, *General Relativity and Gravitation* **40** (2007) 357.
- [22] T.P. Sotiriou and V. Faraoni,  *$f(r)$  theories of gravity*, *Reviews of Modern Physics* **82** (2010) 451.
- [23] T. Koivisto and H. Kurki-Suonio, *Cosmological perturbations in the palatini formulation of modified gravity*, *Classical and Quantum Gravity* **23** (2006) 2355.

- [24] T. Koivisto, *Matter power spectrum in  $f(r)$  gravity*, *Phys. Rev. D* **73** (2006) 083517.
- [25] T. Harko, T.S. Koivisto, F.S.N. Lobo and G.J. Olmo, *Metric-palatini gravity unifying local constraints and late-time cosmic acceleration*, *Physical Review D* **85** (2012) 084016.
- [26] S. Capozziello, T. Harko, T. Koivisto, F. Lobo and G. Olmo, *Hybrid metric-palatini gravity*, *Universe* **1** (2015) 199.
- [27] T. Harko and F.S.N. Lobo, *Beyond einstein's general relativity: Hybrid metric-palatini gravity and curvature-matter couplings*, *International Journal of Modern Physics D* **29** (2020) 2030008.
- [28] C.G. Böhmer, F.S.N. Lobo and N. Tamanini, *Einstein static universe in hybrid metric-palatini gravity*, *Physical Review D* **88** (2013) 104019.
- [29] N.A. Lima, V. Smer-Barreto and L. Lombriser, *Constraints on decaying early modified gravity from cosmological observations*, *Physical Review D* **94** (2016) 083507.
- [30] S. Capozziello, T. Harko, T.S. Koivisto, F.S. Lobo and G.J. Olmo, *Cosmology of hybrid metric-palatini  $f(x)$ -gravity*, *Journal of Cosmology and Astroparticle Physics* **2013** (2013) 011.
- [31] I. Leanizbarrutia, F.S. Lobo and D. Sáez-Gómez, *Crossing SNe ia and BAO observational constraints with local ones in hybrid metric-palatini gravity*, *Physical Review D* **95** (2017) 084046 [1701.08980].
- [32] P.I. Dyadina, S.P. Labazova and S.O. Alexeyev, *Post-newtonian limit of hybrid metric-palatini  $f(r)$ -gravity*, *Journal of Experimental and Theoretical Physics* **129** (2019) 838.
- [33] P.I. Dyadina, N.A. Avdeev and S.O. Alexeyev, *Horndeski gravity without screening in binary pulsars*, *Monthly Notices of the Royal Astronomical Society* **483** (2018) 947.
- [34] N.A. Avdeev, P.I. Dyadina and S.P. Labazova, *Test of hybrid metric-palatini  $f(r)$ -gravity in binary pulsars*, *Journal of Experimental and Theoretical Physics* **131** (2020) 537.
- [35] S. Capozziello, T. Harko, T.S. Koivisto, F.S. Lobo and G.J. Olmo, *Galactic rotation curves in hybrid metric-palatini gravity*, *Astroparticle Physics* **50-52** (2013) 65.
- [36] P.I. Dyadina, *Polarization and speed of gravitational waves in hybrid metric-palatini  $f(r)$ -gravity*, *Journal of Experimental and Theoretical Physics* **135** (2022) 333.
- [37] H.R. Kausar, *Gravitational wave solutions in hybrid metric-Palatini theory*, *Astrophys. Space Sci.* **363** (2018) 238.
- [38] K.A. Bronnikov, S.V. Bolokhov and M.V. Skvortsova, *Hybrid metric-palatini gravity: Black holes, wormholes, singularities, and instabilities*, *Gravitation and Cosmology* **26** (2020) 212.
- [39] B. Dănilă, T. Harko, F.S. Lobo and M.K. Mak, *Spherically symmetric static vacuum solutions in hybrid metric-palatini gravity*, *Physical Review D* **99** (2019) 064028.
- [40] S. Capozziello, T. Harko, T.S. Koivisto, F.S.N. Lobo and G.J. Olmo, *Wormholes supported by hybrid metric-palatini gravity*, *Physical Review D* **86** (2012) 127504.
- [41] N.I. Shakura and R.A. Sunyaev, *Black holes in binary systems. observational appearance.*, *Astronomy and Astrophysics* **24** (1973) 337.
- [42] D.N. Page and K.S. Thorne, *Disk-accretion onto a black hole. time-averaged structure of accretion disk*, *Astrophys.J.* **191** (1974) 499.
- [43] I.D. Novikov and K.S. Thorne, *Astrophysics of black holes.*, in *Black Holes (Les Astres Occlus)*, pp. 343–450, Jan., 1973, <https://ui.adsabs.harvard.edu/abs/1973blho.conf..343N>.
- [44] T. Harko, Z. Kovács and F.S.N. Lobo, *Thin accretion disk signatures of slowly rotating black holes in hořava gravity*, *Classical and Quantum Gravity* **28** (2011) 165001.
- [45] M. Heydari-Fard and H.R. Sepangi, *Thin accretion disk signatures of scalarized black holes in einstein-scalar-gauss-bonnet gravity*, *Physics Letters B* **816** (2021) 136276.

- [46] T. Harko, Z. Kovács and F.S.N. Lobo, *Thin accretion disk signatures in dynamical chern–simons-modified gravity*, *Classical and Quantum Gravity* **27** (2010) 105010.
- [47] C.S.J. Pun, Z. Kovács and T. Harko, *Thin accretion disks in  $f(r)$  modified gravity models*, *Physical Review D* **78** (2008) .
- [48] D. Pérez, G.E. Romero and S.E.P. Bergliaffa, *Accretion disks around black holes in modified strong gravity*, *Astronomy & Astrophysics* **551** (2013) A4.
- [49] D. Pérez, F.G.L. Armengol and G.E. Romero, *Accretion disks around black holes in scalar-tensor-vector gravity*, *Physical Review D* **95** (2017) .
- [50] K.S. Thorne, *Disk-Accretion onto a Black Hole. II. Evolution of the Hole*, *Astrophysical Journal* **191** (1974) 507.
- [51] D.F. Torres, *Accretion disc onto a static non-baryonic compact object*, *Nuclear Physics B* **626** (2002) 377.
- [52] J.P. Luminet, *Image of a spherical black hole with thin accretion disk.*, *Astronomy and Astrophysics* **75** (1979) 228.
- [53] B. Bertotti, L. Iess and P. Tortora, *A test of general relativity using radio links with the Cassini spacecraft*, *Nature* **425** (2003) 374.
- [54] X. Zhao, L. Gou, Y. Dong, Y. Tuo, Z. Liao, Y. Li et al., *Estimating the black hole spin for the x-ray binary maxi j1820+070*, *The Astrophysical Journal* **916** (2021) 108.

